IN-VIVO TRACING OF VAGAL PROJECTIONS IN THE BRAIN WITH MANGANESE ENHANCED MAGNTIC RESONANCE IMAGING

by

Steven Oleson

A Thesis

Submitted to the Faculty of Purdue University

In Partial Fulfillment of the Requirements for the degree of

Master of Science in Biomedical Engineering

Weldon School of Biomedical Engineering

West Lafayette, Indiana

December 2018

THE PURDUE UNIVERSITY GRADUATE SCHOOL
STATEMENT OF COMMITTEE APPROVAL

Dr. Zhongming Liu, Chair

Department of Biomedical Engineering

Dr. Preeti Sivasankar

Department of Speech, Language, and Hearing Sciences

Dr. Terry Powley

Department of Psychological Sciences

Approved by:

Dr. George R. Wodicka

Head of the Graduate Program

To my mother, Kim Oleson, who inspired me to study the complex field of biomedical engineering and to never settle for less. And to my father, Tom Oleson, for encouraging me through all of the challenges that I have and will overcome.

ACKNOWLEDGMENTS

First and foremost, I would like to thank my colleagues in the Laboratory of Integrated Brain Imaging (LIBI) Lab. This work would not be possible without their support. I have truly learned more about hard work and dedication than I can ever imagine. Some of my greatest memories throughout graduate school were created by the sides of these people. Specifically, I will never forget the experiences and sites that the ISMRM crew (Tom Lu, Ranajay Mandal, and Nishant Babaria) and I were able to share when we traveled to France. I would also like to thank my mentor and friend, Dr. Zhongming Liu, for the inspiration and willingness to let me grow and learn as part of such a magnificent group. The opportunity of being able to pursue a graduate level education means the world to me. I will forever strive to aim big.

There are multiple professors that I got the pleasure of learning from who I would like to thank. I would like to thank Dr. Preeti Sivasankar for her trust and leadership when tackling complex problems. Being able to learn concepts outside of my background has opened up a new and improved way of thinking for me. I also want to thank Dr. Abigail Durkes, whose great knowledge of tissue and veterinary sciences was vital in my learning. The experience I gained when writing the vocal fold publication and attending COSM is truly incredible. Furthermore, I would like to thank Dr. Terry Powley for his expertise in tracing technologies. His input and in-depth advice, along with the help of his laboratory team, helped me explore new areas of analysis and future ideas for this thesis.

All of the technical techniques that were used throughout this thesis were taught to me from Tom Lu and Cherry Cao. When I first joined LIBI Lab, I was an undergraduate and looking to get my hands dirty in academic research. I could have never predicted that I would end up learning MRI operation, surgical techniques, or data-driven analysis. I want to thank Tom for his generosity and patience when teaching me concepts such as statistical approaches and image analysis. Additionally, I will miss our in-depth conversations that we had during long MRI sessions about experiments, career plans, and funny stories. I want to thank Cherry for answering all of my questions related to the vagal and brain anatomy. I would not have been able to finish this work without their help.

Thank you again for all of the mentoring and support throughout the years.

TABLE OF CONTENTS

LIST OF TABLES

LIST OF FIGURES

LIST OF ANATOMICAL ABBREVIATIONS

vagus nerve nucleus (10N)

central canal (CC)

solitary tract (sol)

solitary nu, commissural part (SolC)

solitary nu, dorsolateral part (SolDL)

solitary nu, interstitial part (SolI)

solitary nu, intermediate part (SolIM)

solitary nucleus, medial part (SolM)

solitary nu, ventral part (SolV)

solitary nu, ventrolateral part (SolVL)

ABSTRACT

Author: Oleson, Steven, T. MS
Institution: Purdue University
Degree Received: December 2018
Title: In-vivo Tracing of Vagal Projections in the Brain with Manganese Enhanced Magnetic Resonance Imaging
Committee Chair: Zhongming Liu

Current challenges in neuronal tract tracing include sacrificing the animal, detailed sectioning of the brain, and cumbersome reconstruction of slices to gather information, which are very tedious, time consuming, and have low-throughput. In this regard, Manganese-enhanced Magnetic Resonance Imaging (MEMRI) has been an emerging methodology for fiber tract tracing *in vivo*. The manganese ion (Mn^{2+}) is paramagnetic and is analogous to calcium ions (Ca^{2+}), which allows it to enter excitable cells through voltage-gated calcium channels, thereby reporting cellular activity in T_1-weighted MR images. Moreover, once the Mn^{2+} enters the cell, it will move along the axon by microtubules, release at the synapse, and then uptake by post-synaptic neurons, hence revealing the pathway of Mn^{2+} transportation. While most MEMRI neuronal tracing studies have focused on mapping circuitries within the brain, MEMRI has rarely been applied to trace peripheral nerve projections into the brain.

In this thesis, I will propose the use of MEMRI to trace vagal nerve projections into the central nervous system by showing enhancement of neuronal pathways with an optimized protocol. This protocol demonstrates *in vivo* monitoring of manganese transport into the brain from the nodose ganglion and shows how the enhancement in MR images can be promoted with vagus nerve stimulation (VNS). Additionally, I will present preliminary findings, for the very first time, that show the downstream projection of the sympathetic pathway from the brainstem. In sum, the technique presented in this thesis will shed light on the use of MEMRI to study the functional results of using clinically-based VNS settings.

1. INTRODUCTION

1.1 Functional Activation of Parasympathetic System

The autonomic nervous system (ANS) controls many of the bodily functions that do not need to be consciously thought of in order to work. Specifically, there are two components within the ANS: the sympathetic and parasympathetic systems. These components of the control and regulate the function of many different organs within the body. Some of these functions are heart rate, respiration, vocalization, and gastric secretion [1]. Furthermore, within the parasympathetic system, the vagus nerve acts as the connection between the brain and specific body organs like the lungs, stomach, and intestines. The vagus nerve consists of a mix of about 20% efferent fibers that transport signals from the brain to the body, and about 80% afferent fibers that transport signals from different body organs to the brain for regulation of the ANS.

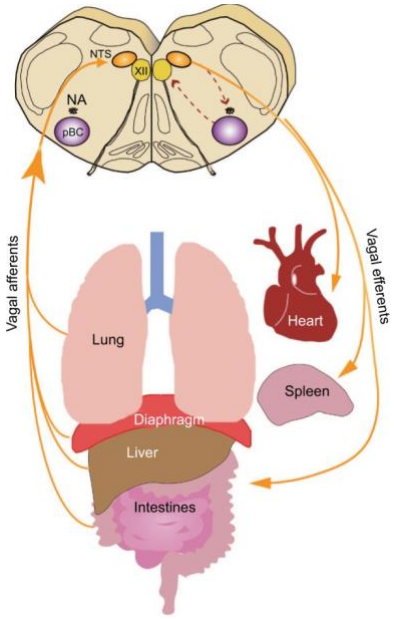

Figure 1. The parasympathetic system.

Researchers have been studying the therapeutic effects of using a method called vagal nerve stimulation (VNS) for brain and peripheral diseases like epilepsy and depression [2]. Additionally, this method has been studied for its use to combat the effects of inflammatory diseases like arthritis, cardiovascular disease, and Alzheimer's Disease (AD). VNS has FDA

approval for limited clinical applications, but is mostly used in preclinical studies. This technique uses electrodes implanted around the vagus nerve, typically the left vagus nerve, which then sends electrical signals along the nerve and into the brain. VNS can be utilized to activate different functional pathways within the brain depending on the specific stimulation parameters that are used. Currently, we know that the brain stem plays an important role in integration of signals between the CNS and the vagus nerve, but we have incomplete knowledge of how VNS modulates the central nervous system (CNS) [2]. Often times when a patient is having their VNS parameters programmed, these parameters are changed based on the patients' reaction to adverse effects like throat pain or tingling sensations. Therefore, VNS parameters are primarily determined based on trial and error because it has been a challenge to understand how specific VNS parameters affect specific brain pathways. One method that has great potential for studying the activated, functional pathways of the vagus nerve during stimulation is Manganese Enhanced Magnetic Resonance Imaging (MEMRI). This method could be used to give possible answers for how different VNS parameters affect the brain.

1.2 The Basics of Magnetic Resonance Imaging

Magnetic resonance imaging has long been established as a great *in-vivo* technique for assessing anatomical architecture and functional changes within the body. In order to fully appreciate the work and results shown within this thesis, it is important to understand the basics of MRI. Here, I will explain them.

The human body is mainly comprised of hydrogen nuclei that consist of a single proton, which carries a positive electrical charge [3]. Each proton is constantly spinning, which creates a current, and a resulting magnetic field. Thus, protons have their own magnetic fields and behave like little bar magnets. This can be visualized in Figure 2.

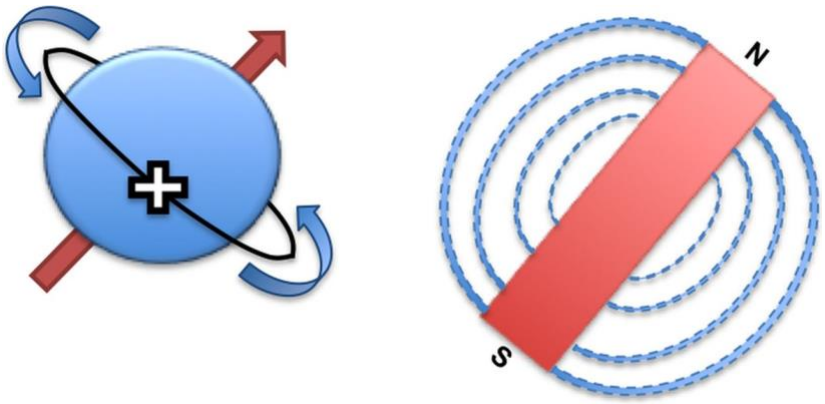

Figure 2. Protons are always spinning about their axis and are similar to little bar magnets

All of these small magnetic fields within the body spin randomly. When the body is placed within a large, external magnetic field (β_0,), the protons within the body are then aligned either parallel or antiparallel to the external field. A larger portion of the protons align parallel with β_0, which is at a lower energy state than aligning antiparallel. As the strength of β_0 increases, the number of protons that align parallel also increases. Additionally, these aligned protons spin in a specific manner that is called precession. This is often compared to the movement of a spinning top. The top of the proton wobbles and forms a cone-like shape [3] as shown in Figure 3.

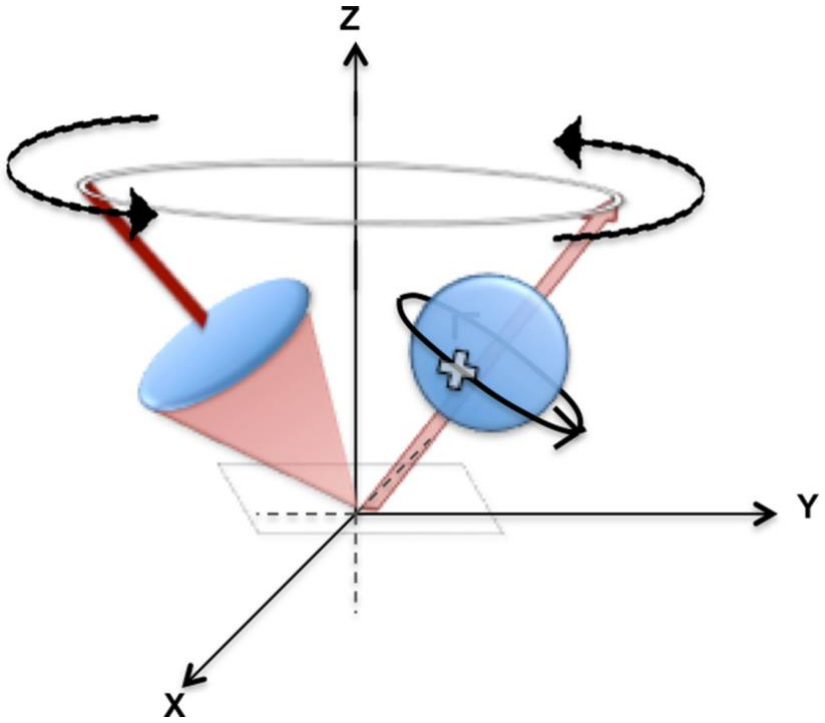

Figure 3. Protons precess in a manner that is similar to a spinning top when they are aligned in an external magnetic field.

This precession is measured as the Larmor frequency (ω_0, in MHz) and determines how many times the protons precess per second. The Larmor frequency can also be expressed in the following equation:

$$\omega_0 = \gamma\beta_0 \qquad (1.1)$$

γ is a constant for the gyromagnetic ratio and β_0 is the external magnetic field. Because there are a surplus of protons precessing parallel to β_0 compared to antiparallel, they cancel each other out in all directions, except for the direction of the aligned magnetic field [3]. This is termed longitudinal magnetization.

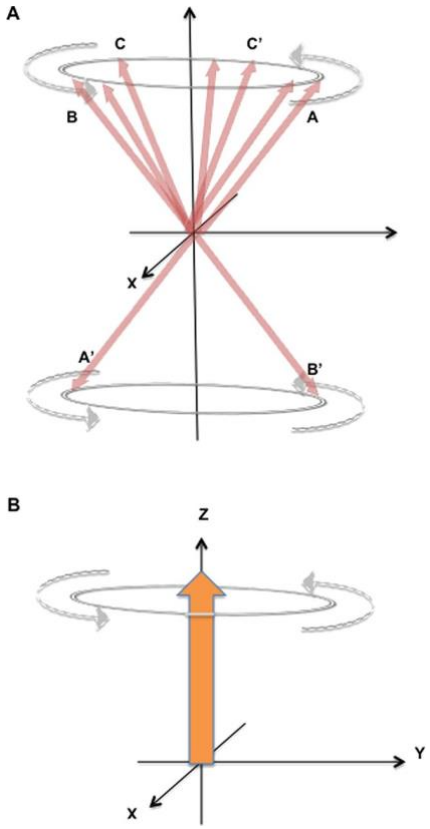

Figure 4. Diagram showing the longitudinal magnetization of protons.

(A). The opposing protons precessing in the external magnetic field cancel each other out. (B). The resulting magnetization is aligned in primarily one direction, along the z-axis. The longitudinal magnetization of the protons are drawn as vectors.

Figure 4 illustrates that when an object is placed within the middle of an MRI scanner, the sum magnetization acts similar to a magnet that is aligned with β_0. The randomly precessing protons cancel each other out, and the resulting magnetization is along the z-axis. Once an object is placed within the magnet, radio frequency (RF) pulses at Larmor frequency are turned on an off in order to disturb the protons out of alignment with β_0. When the protons are disturbed by the RF pulse, one main effect occurs: the protons are aligned in phase with each other at a higher energy state. This means that they are now precessing in the same direction simultaneously, which is termed transverse magnetization. The transverse magnetization also occurs at Larmor frequency. Then, once the RF pulse is switched off, the protons start to fall out of phase with each other and relax back to their lower energy state. This relaxation can be measured in two different ways: T_1 relaxation and T_2 relaxation. T_1 relaxation is the process of the protons

returning to their longitudinal direction, and T_2 relaxation is the process of the protons precessing out of phase with each other [3]. In order to quantify these processes, T_1 is defined as the time required for the z-component of the magnetization to reach 63% (1 – 1/e) of its maximum value [4], and T_2 relaxation is the time required for the transverse magnetization to fall to approximately 37% (1/e) of its initial value [5]. This process can be visualized in Figure 5.

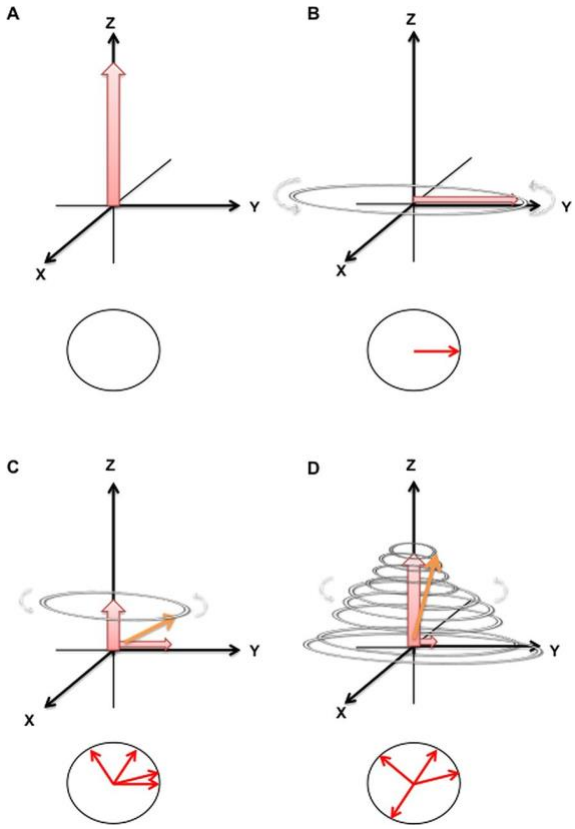

Figure 5. The effects of an RF pulse on protons.

(A) Protons are primarily aligned with β_0, resulting in magnetization in one direction. (B) After an RF pulse is turned on, the protons are tipped down into the x-y plane, called a 90° flip. (C) Once the RF pulse is turned off, the protons start to fall out of phase with each other, which is portrayed as multiple vectors. (D) The protons eventually recover from the RF pulse and relax back to the z-axis (T_1), while also becoming further out of phase with each other (T_2) [3].

The magnetization relaxation for each proton is a moving magnetic field. Thus, a conductive receiver coil can be placed within proximity to induce an alternating voltage. This generates an electrical current, which can be picked up in the form of an MR signal. Additionally, different molecules have different relaxation times. Thus, they give off different

MR signals, which show up as different levels of intensities within an MR image. This contrast between adjacent tissues enables us to differentiate them.

When an RF pulse is switched off, T_1 and T_2 relaxation occur simultaneously and independently. The resulting magnetization vector goes in a spiraling path, where its direction and magnitude are constantly changing. The MR signal generated from this magnetization vector is called free induction decay (FID) [3]. The maximum magnitude occurs immediately after the RF pulse is turned off and decreases as both longitudinal and transverse relaxation occur.

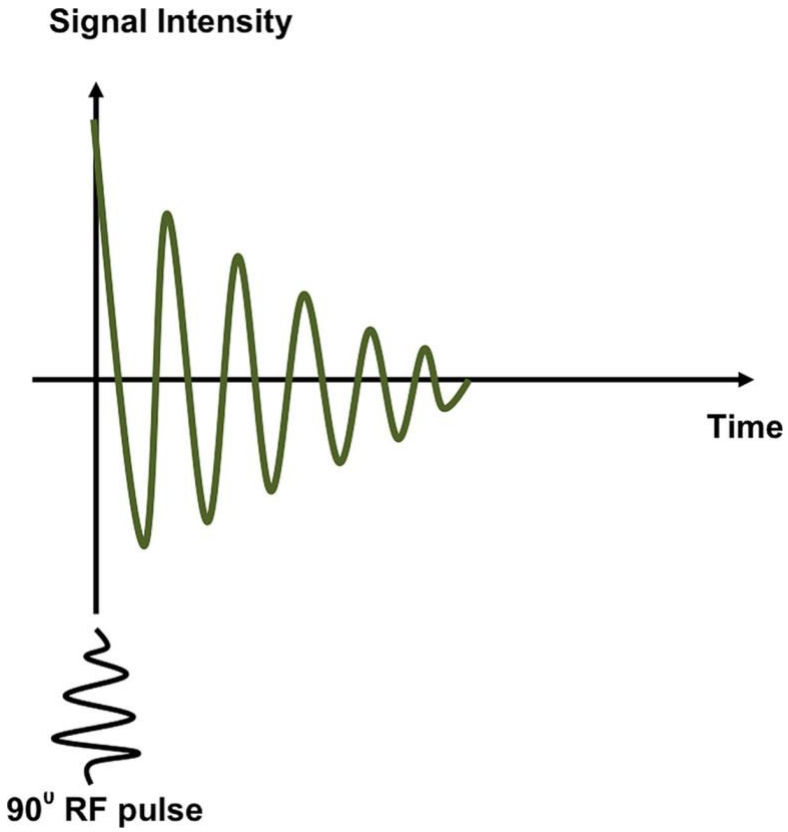

Figure 6. Free induction decay plot.

By varying the sequence of RF pulses that are applied and collected, different types of images are created. Repetition time (TR) is the amount of time between successive RF pulses. Echo time (TE) is the time between the delivery of the RF pulse and the peak of the echo signal induced in the coil [6]. An image in which the difference in signal intensity between tissues is predominantly due to differences in T_1 relaxation time is called a T_1-weighted image [3]. This is produced by using short TE and TR times. Furthermore, T_2-weighted images are produced by

using longer TE and TR times, and the signal intensity is predominately determined by the T_2 properties. An example of one way to categorize a T_1 and T_2-weighted image is by looking at the cerebral spinal fluid (CSF) within the brain. The CSF is dark in a T_1-weighted image, and bright in a T_1-weighted image.

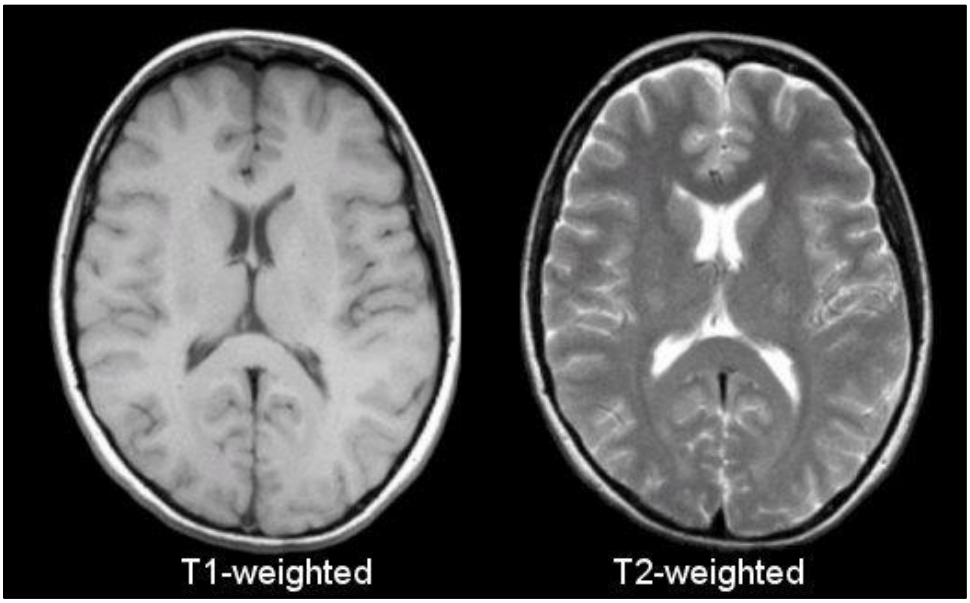

Figure 7. Comparison of a T_1 and T_2-weighted MR image of the brain.
The CSF is dark in the T_1-weighted image, and bright in the T_2-weighted image.

It is important to note that the complete physics of MRI are much more complex than what has been explained. Going into further depth and more complex MRI physics is out of the scope of this thesis.

1.3 Tract-Tracing Methodologies

Tract-tracing methodologies have contributed a large amount of information to our current understanding of neuronal connections and pathways. These traditional techniques involve using a detectable tracer that is able to transport along neurons, either retrograde or anterograde. Retrograde tract tracers travel towards the soma of a neuron where they accumulate. Anterograde tract tracers travel away from the soma along axons toward synaptic terminals [7]. Some examples of tract tracing methodologies have used tracers such as biotinylate dextran,

horseradish peroxidase, fluorogold, herpes simplex virus, and molecular genetic expression. Biotinylate dextran is a novel analogue of biotin, and can act as both a retrograde and anterograde tracer [8]. This tracer can be detected with avidin-conjugated marker for light or electron microscopy studies to study axon terminals, dendrites, and even dendritic spines. Horseradish peroxidase is a protein tracer that has sensitive localization with light and electron microscopy. This tracer was used to show that an exogenous protein can transport retrogradely within the central nervous system (CNS) [9]. Another retrograde tract tracer is fluorogold. Fluorogold is a fluorescent tracer, which has been used to examine the cell origins of afferent projections within the brain [10]. A tracer that can act as either an anterograde or both an anterograde and retrograde tracer, is Herpes simplex virus (HSV), which has been utilized to trace the movement from the retina to subcortical regions [11]. HSV can even cross synapses to trace networks of neuronal connections. Molecular genetic techniques can also be used as tracers. A genetic approach was developed to visualize the anterograde transport of axons expressing a given odorant receptor in mice [12].

Although traditional tract tracing techniques have contributed to the discoveries of many scientific breakthroughs, they all have a similar disadvantage: they all require the sacrifice of the animal. Once the animal is sacrificed, the brain has to be fixed, removed, sectioned, and stained in order to visualize the transport. Additionally, they require the reconstruction of sequential sections to get three-dimensional visualization, which is extremely inefficient, time consuming, and tedious [7]. These methods are also unable to trace functional pathways that are activated through techniques like vagus nerve stimulation. Therefore, an *in-vivo* approach for tract tracing is needed that is able to visualize functional activity.

1.4 Manganese Enhanced Magnetic Resonance Imaging

The method that I used to overcome the limitations of traditional tract tracing techniques is Manganese Enhanced Magnetic Resonance Imaging (MEMRI). MEMRI is a developing technique that uses the unique properties of the manganese (Mn^{2+}) ion. One of its unique properties is that Mn^{2+} is a paramagnetic contrast agent and is able to shorten the T_1 and T_2 relaxation times in MRI. This means that Mn^{2+} accumulation shows up as bright in T_1-weighted MR images and can be easily visualized [13][14]. Another one of Mn^{2+}'s unique properties is that it has a similar biophysical shape to calcium (Ca^{2+}), so it is able to act as a Ca^{2+} analogue.

This means that it can enter excitable cells through voltage-gated Ca^{2+} channels. Once in excited cells, Mn^{2+} can transport along axons via microtubule-dependent transport, release at the synapse, and uptake by adjacent post-synaptic neurons to continue transport along the neuronal circuit [15]. Therefore, MEMRI has great potential for studying the activated, functional pathways of the vagus nerve during stimulation and can be used to visualize functional activity.

1.5 Early Investigations Using Manganese

After manganese (Mn^{2+}) was presented as a possible tracer because of its ability to be uptake and transport within neurons, Narita et al. demonstrated that Mn^{2+} was able to act as a Ca^{2+} analogue. They showed some of the first results of Mn^{2+} entering neurons via voltage gated Ca^{2+} channels [16]. Additionally, it was demonstrated with autoradiography that after $Mn^{2+}$was applied to the naris of northern pike fish it accumulated in the olfactory bulbs as well as in parts of the telencephalon and diencephalon [17]. Multiple studies also demonstrated these results in the rat model [18][19] and even injected Mn^{2+} into the basal ganglia where it transported to other brain regions [20]. When colchicine was administered as an external application, transportation of Mn^{2+} was blocked, which indicated that Mn^{2+} transport is dependent on microtubules. Colchicine is able to bind to tubulins, thereby blocking assembly and polymerization of microtubules [21]. Although the main scope of these studies was focused on the biodistribution of Mn^{2+}, it was evident that Mn^{2+} had promise for use as a tract tracer.

As stated earlier, one of Mn^{2+}'s unique properties is that it is paramagnetic and acts as a contrast agent for MR images. Therefore, when Mn^{2+} accumulates in specific locations, it shows up as a positive contrast for T_1-weighted MR images [13][14]. However, when it accumulates at high concentrations, there is a signal loss due to extreme T_2 shortening. In one of the early applications using Mn^{2+} as an *in-vivo* contrast agent for MRI, Cory et al. demonstrated the loss in signal from higher concentrations of Mn^{2+} when investigating its contrast abilities in the rat gastrointestinal tract [14]. At a low solution concentration, they showed that the stomach could be observed as bright, whereas when the dose was increased by 100x, the stomach was observed as dark.

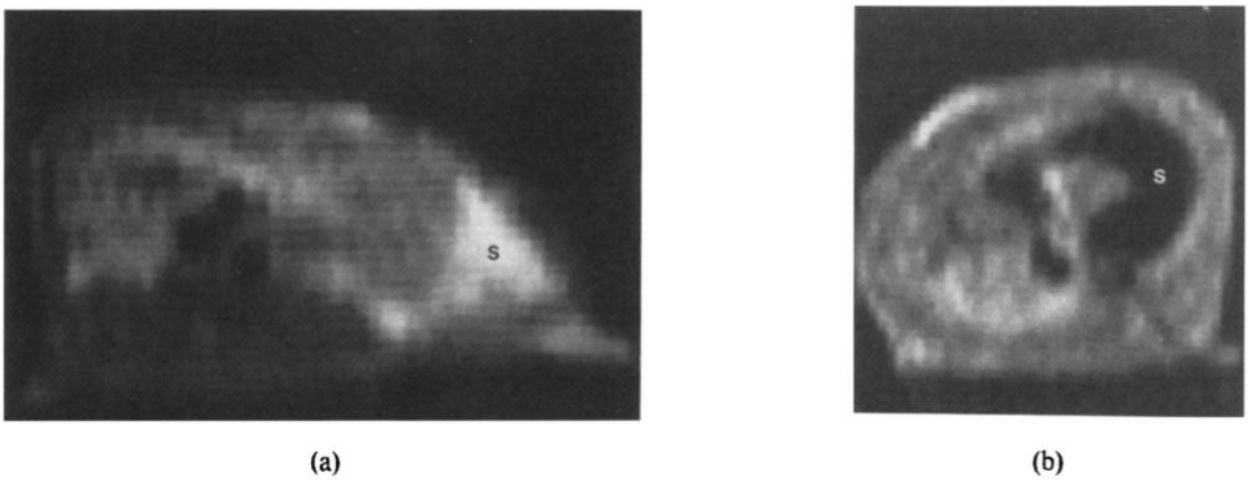

Figure 8. Early demonstration of manganese used as a contrast agent.

(A). A T_1-weighted MR image of a rat stomach marked with an 's'. The rat received a 1.0mM solution of manganese chloride. (B). A T_1-weighted MR image of a rat stomach marked with an 's'. The rat received a 100mM solution of manganese chloride.

1.6 The Beginning of MEMRI For Neuronal Tract Tracing

Mn^{2+} was first demonstrated as a neuronal tract tracer for MRI applications in a 1998 publication by Alan Koretsky and colleagues [7]. Specifically, they showed the feasibility of using Mn^{2+} to trace the murine olfactory and visual pathways. Their technique consisted of topically administering $MnCl_2$ to the naris and injecting $MnCl_2$ into the vitreous humor of the eye to highlight the specific neuronal sensory pathways of the live mice. They were able to trace enhancement from the olfactory epithelium to the heterogeneous enhancement of the olfactory bulb, and from the vitreal humor to its optical tract and contralateral superior colliculus. This demonstrated the specificity of using Mn^{2+} to trace different sensory pathways in the brain, and showed the potential for using Mn^{2+} as an *in-vivo* MRI-detectable tract tracer.

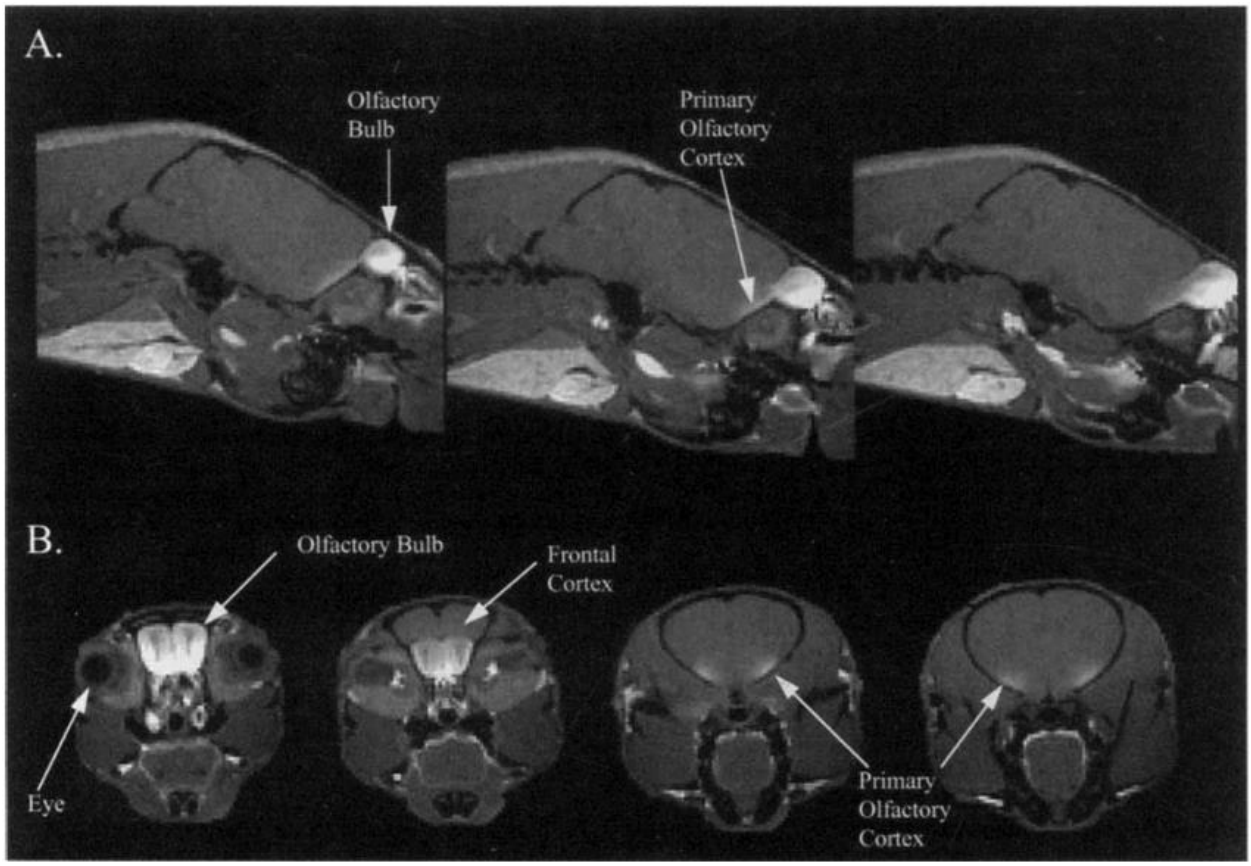

Figure 9. T_1-weighted MR images demonstrating olfactory pathway enhancement. (A). Sagittal slices showing the enhanced olfactory bulb and primary olfactory cortex. (B). Axial slices showing the enhancement of the outer layers of the olfactory bulbs, where the olfactory glomeruli are located. The enhancement is also in the primary olfactory cortex.

In the work presented in Figure 9, Pautler et al. demonstrated that the injected Mn^{2+} transported anterograde and crossed a synapse in order for the resulting enhancements to have occurred. This work demonstrated transport across a synapse because the secondary olfactory neurons and the primary olfactory cortex have a synapse between their connection and both sites were enhanced [7]. Around the same time, Lin and Koretsky released work that showed Mn^{2+} was able to accumulate in an activity-dependent fashion using glutamate stimulation [22]. Activation of the brain with glutamate led to an increase in MRI signal intensity in the brain compared to the original signal intensity. This meant that Mn^{2+} transport was changed based on stimulation intervention. Therefore, the groundwork was laid for using Mn^{2+} to not only trace anatomical connections, but also activity-dependent functional connections. Takeda et al. even showed results observing that Mn^{2+} corelease with neurotransmitters [23].

1.7 MEMRI Applications

Since the foundation of establishing Mn^{2+} as a neuronal tract tracer, there have a lot of interesting applications when using Mn^{2+}. Here, I will dive into the vast history of MEMRI and its uses for different studies.

In 2002, Pautler et al. [24] combined the tract tracing properties of Mn^{2+} [7] with its activity dependence properties [22] to show that aerosolized Mn^{2+} can selectively accumulate within the olfactory bulbs of mice based on various odor stimuli.

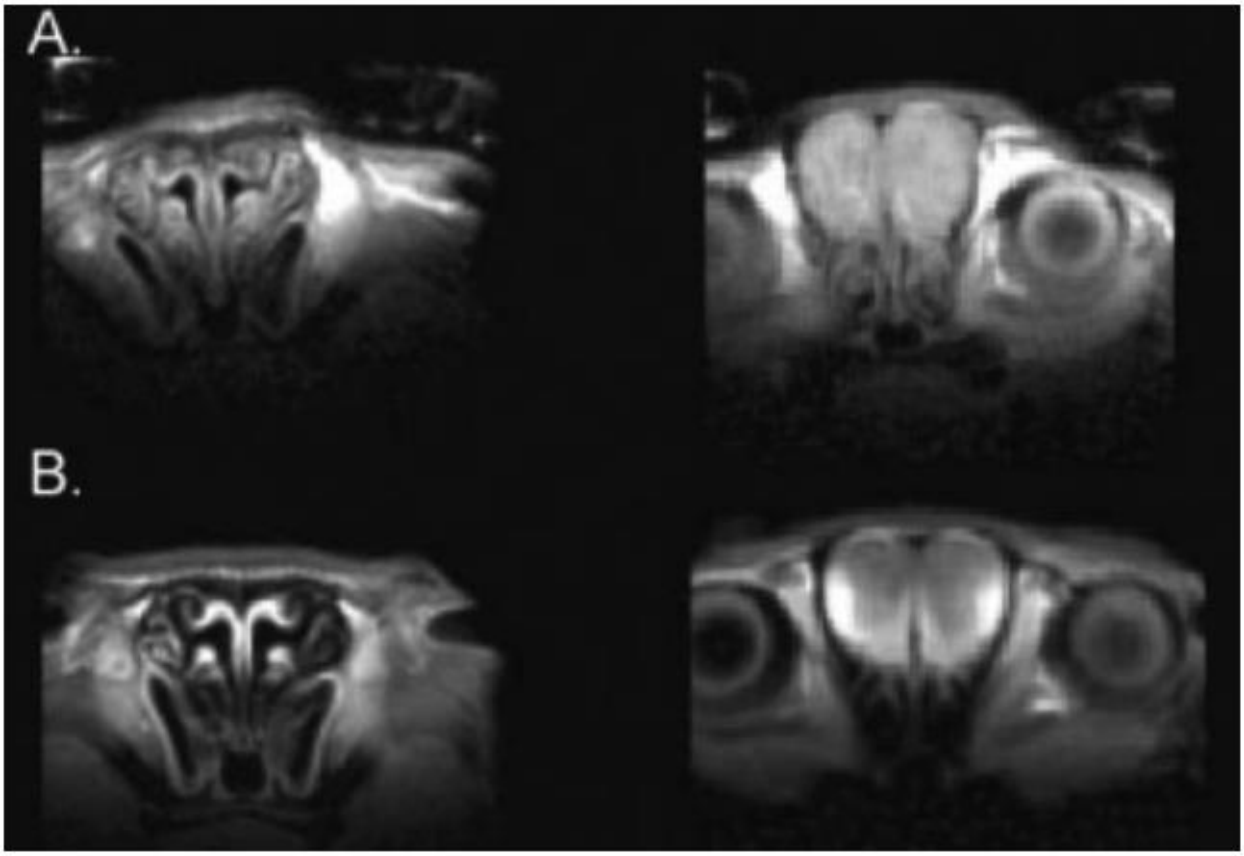

Figure 10. Activity-dependent MEMRI tract-tracing in response to olfactory activation. (A). Control mice 1.5 hours after being exposed to aerosolized Mn^{2+}. (B). Mice 1.5 hours after being exposed to aerosolized Mn^{2+} and amyl acetate. The left column are turbinates and the right column is the olfactory bulb. Notice the differences in enhancement pattern based on smell.

Van Der Linden et al. used an injection of Mn^{2+} into the high vocal center of starlings to trace the transportation and functional properties of the vocal-control system. They were even

able to compare sex differences [25]. At the same time, Saleem et al. showed transport of Mn^{2+} from the striatum to the pallidum-substantia nigra and then to the thalamus in the monkey, which supported evidence of transport across at least one synapse within the CNS [26]. In 2003, Allegrini and Wiessner investigated the potential of tracing neuronal projections originating in the sensorimotor cortex in healthy and lesioned rat brains [27]. Excitement for MEMRI was increasing and two different review articles were released in 2004: one by Silva et al. [28] and the other by Pautler [15]. Both of these review articles focused on the three different types of applications when using MEMRI: activation-induced MRI (AIM-MRI), neuronal tract tracing, and systemic administration of Mn^{2+}.

1.7.1 Using MEMRI for Toxicity Studies

One of the downfalls of MEMRI is that it relies on the application of Mn^{2+}, which is a toxic contrast agent. Olanow reported that Mn^{2+} exposure can cause a neurologic syndrome that resembles Parkinson's disease, but that the effects could be differentiated based on the location of accumulation [29]. Acute overexposure of Mn^{2+} had also been long reported, leading to adverse effects such as hepatic failure [30] and cardiac toxicity [31]. Because of this toxicity, it is imperative to minimize the dose of the Mn^{2+} used for every study. However, minimizing the dose is also a tradeoff, because the effective relaxation rate is directly proportional to the concentration of Mn^{2+} within the localized tissue [28]. Cell labeling for MEMRI with $MnCl_2$ was investigated by Aoki et al. in 2006 [32]. Part of their study showed that T_1-weighted MRI signal intensity could be significantly enhanced when human lymphocytes were submerged in low concentrations of $MnCl_2$. The low concentrations did not affect cell viability, but *in vitro* concentrations of greater than 2mM Mn^{2+} were toxic due to disruption of cells.

1.7.2 Using MEMRI for Brain Plasticity Studies

The potential in using MEMRI to study brain plasticity has been investigated. Specifically, Tindemans et al. showed that MEMRI could assess the functional state of specific neuronal populations in the song system of living canaries. They demonstrated that song stimulation specifically affected the uptake of Mn^{2+} for specific projection neurons [33]. Then, a year later, Van Meir et al. published work showing that testosterone was able to differentially

affect specific projection neurons in songbirds [34]. These works showed the abilities of using MEMRI to assess slow time scale functional connectivity changes in brain activity and plasticity.

Paulo de Sousa et al. were able to give more insights into using MEMRI when studying brain development. They presented that Mn^{2+} concentrations were higher in early postnatal rats and decreased with brain maturity. Their work also showed no significant differences in T_1 value amounts of different brain regions in the neonate rats. This was perhaps due to an unformed blood brain barrier (BBB) or because the developing brain is a relatively homogeneous structure in terms of cellular densities and neuronal activity compared to the adult brain [35].

1.7.3 Using MEMRI for Single Animal Analyses

Single animal analyses were investigated with MEMRI. Simmons et al. introduced work showing that MEMRI could be used to map distributions of multiple neuronal circuits in a single monkey. They were able to compare between striatal projections from the orbitofrontal cortex and the anterior cingulate cortex. Manganese is known to be visible in axonal fibers and synaptic terminals, so they used another method of confirmation to differentiate them with higher spatial resolution. Their paper presented ideas for using MEMRI alongside functional MRI to superimpose connectivity maps onto correlated maps of brain activity patterns [36], all in the same animal.

1.7.4 Using MEMRI for Task Based Studies

MEMRI gained interest when being applied for task-based studies as well. Yu et al. published a study in *Nature Neuroscience* demonstrating a method that mapped regions of accumulated sound-evoked activity in awake, normal behaving mice [37]. They were able to map the tonotopic organization of the mouse IC when being exposed to defined stimuli of different sound frequencies. These accumulation maps can be seen in Figure 11. This showed that MEMRI was useful for mapping the mouse auditory brainstem and showed the potential for a range of functional neuroimaging studies. Additionally, Kuo et al. showed promising results when using MEMRI to detect hypothalamic function associated with feeding [38]. Specifically, they showed that with a fasting protocol they were able to detect temporal and regional differences of Mn^{2+} enhancement without breaking the BBB.

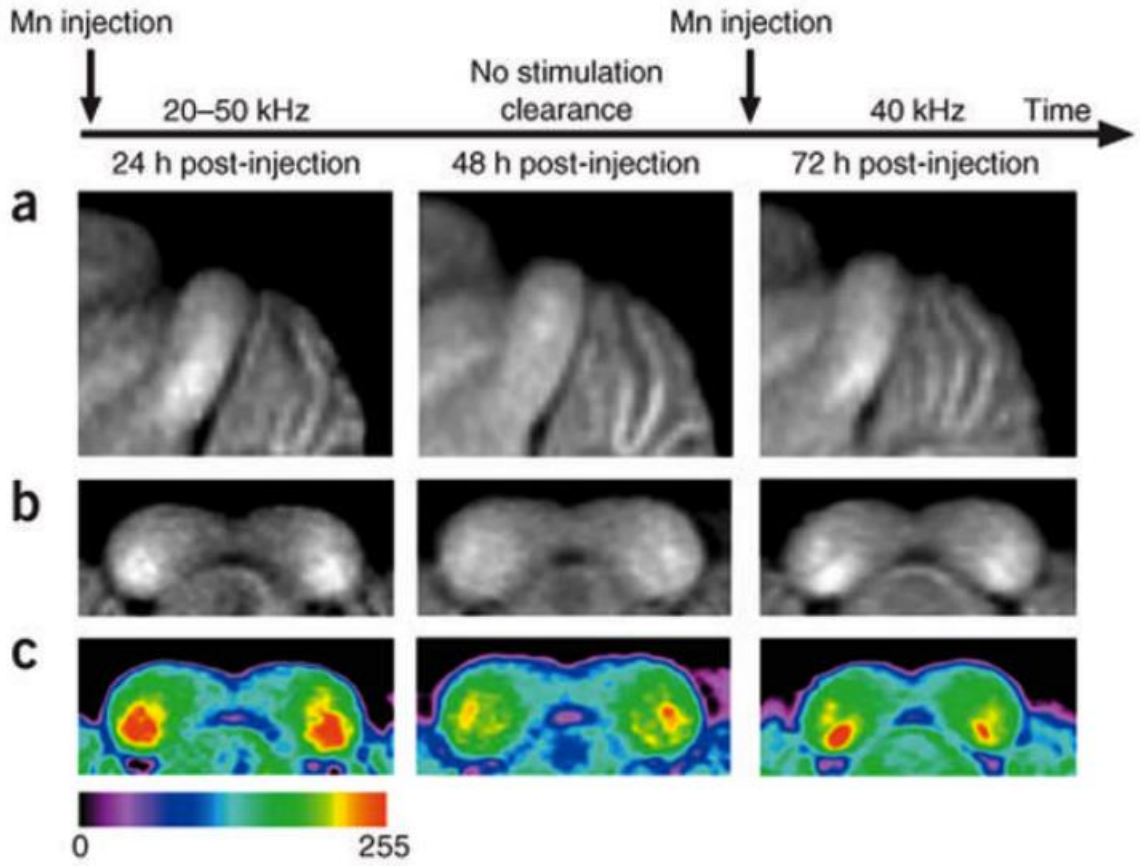

Figure 11. MEMRI for task based and longitudinal studies.

(A). Averaged sagittal and (B). coronal images of the IC after injection of $MnCl_2$ and 24 hours of exposure to 20-50 kHz noise (left), after another 24 hours with no defined stimulation (center), and after a final injection of a half-dose of $MnCl_2$ and exposure to the 40 kHz pure tone for 24 hours (right). (C). Coronal maps in color. Note the specific accumulation within the IC depending on the stimulation.

1.7.5 Using MEMRI for Disease States

Research in using Mn^{2+} as a tract tracer opened up applications for studying different disease states. There was a multitude of studies that applied tract tracing protocols to animal models with different disease states like Alzheimer's disease (AD), stroke, and spinal cord injury. For example, Smith et al. used MEMRI to study the axonal transport rates at various stages of amyloid-beta deposition and plaque formation in the AD model [39], Van der Zijden et al. measured Mn^{2+} accumulation to observe the patterns of enhancement in the sensorimotor cortex of rats with an occluded middle cerebral artery to simulate stroke [40], and Bilgen et al.

applied the MEMRI technique to a rat spinal cord injury model and were able to accurately label functional neurons [41]. These tract tracing studies also showed validated MEMRI results with other tract tracers such as biotinylated dextran amine and wheat-germ agglutinin horseradish peroxidase.

1.7.6 The Specificity of MEMRI

In 2009 it was not clear as to what level of specificity neuronal connectivity could be measured using MEMRI tracing methodologies. Chuang et al. used MEMRI to map the flow of neural information from the olfactory sensory neurons (OSNs) to the central layers of the olfactory bulb. This work produced functional connectivity maps that are consistent with the flow of information from the OSNs to the glomerular and mitral cell layers and had a sensitivity at the level of single glomeruli [42]. Additionally, work was published investigating if MEMRI could distinguish layer inputs of major pathways of the cortex [43]. This work showed layer specific tracings after local injections of $MnCl_2$ and found differences in maximal signal enhancement throughout different depths of the cortex specific to neuronal input pathways. One of the key contributions of this work showed that it was critical to perform MRI at specific times after injection to detect layer specificity. At later time points, tracing of the network let to more uniform contrast throughout the cortex due to complex neuronal connections.

1.7.7 Investigations into the Small Details of MEMRI

As MEMRI has become more of an investigated technique for applications like neuronal tracing, the finer details and specifics about the technique started to be studied and continue to be studied. For example, Maassaad and Pautler authored a chapter in the textbook *Magnetic Resonance Neuroimaging Methods and Protocols* that introduced applications for MEMRI with specific step-by-step procedures for experiments [44]. Pautler's group additionally released review articles on the neurophysiological applications of MEMRI [45] and how to use MEMRI to further understand the blood oxygenation level-dependent (BOLD) contrast signal in functional MRI [46].

Details such as the confounding effects of nonspecific enhancement are also important. Depending on how Mn^{2+} was administered, Mn^{2+} can leak into blood vessels or cerebrospinal fluid (CSF). This results in circulation of the injection and enhancement of brain regions that are

not within the specific pathway. Therefore, it is important to compare time courses of injections with intravenous infusions of Mn^{2+}. Chuang et al. showed that the pituitary gland could be used as an internal reference for systemic effects because of its early enhancement [47] after infusion. This work stated that nonspecific enhancements in MEMRI tract-tracing studies need to be carefully taken into account. Very recent work still investigates the specifics of validating Mn^{2+} and its use as a marker for functional imaging. Svehla et al. recently showed results that neuronal activity (action potentials and bursts of action potentials) is positively correlated with MEMRI signal in single *Aplysia* buccal ganglia [48], but they were unable to correlate MEMRI signal with ongoing synaptic activity leading to Mn^{2+} influx. This showed that the MEMRI signal consisted of mainly fast and high membrane depolarization processes like action potentials. Slow and small membrane depolarizations like post-synaptic potentials had little affect towards manganese transport.

Even the specifics about how manganese transports through different types of calcium channels has been investigated recently. It is now known that the L-type calcium channel 1.2 in the CNS is an important channel for neuronal manganese influx after systemic injections. However, L-type calcium channel 1.3 is not very important [49]. Therefore, the strongest accumulation of manganese is observed in projection terminals of regions with a high density of Ca 1.2 channels.

1.8 Creative Ways to Deliver Manganese

Publications have varied in how Mn^{2+} has been administered within animal studies for *in vivo* detection. These have varied from direct injections into specific regions of the body, to systemic injections. It was demonstrated that there was a dose-dependent and temporal dependence of contrast within the brain when delivering Mn^{2+} systemically to the brain [50]. They concluded that the optimal dose of Mn^{2+} and the time that MRI should be performed after a systemic dose should be determined based on the target region of interest's maximum contrast enhancement.

Some of the most recent works of using MEMRI to study brain function revolved around using creative methods for administering Mn^{2+}. In 2014, Koretsky and colleagues released work on the cellular responses to the acute phase of traumatic brain injury (TBI). Part of this study indicated that the skull bone is permeable to small-molecular-weight compounds [51] and that

the concentration of the diffused molecules into the brain was dependent on the size of the molecule and the length of the application to the skull. Therefore, this showed that specific molecules could be delivered to the brain while leaving the skull intact. This was termed transcranial application. Then in 2017, Koretsky and colleagues published further work determining the factors that affected transcranial Mn^{2+} and if Mn^{2+} applied in this manner could be used for neuronal tracing [52]. Specifically, there was a dependence on the location of the applied solution to the skull based on where skull bone plates come together (e.g. the Bregma), a dependence on the concentration of manganese applied, the effectiveness of manganese delivery increased with the addition of calcium, and the manganese traced to the appropriate neuronal pathways after administration. This work showed the direction that MEMRI studies are moving towards, which is finding creative, less-invasive approaches for brain delivery of contrast agents and drugs.

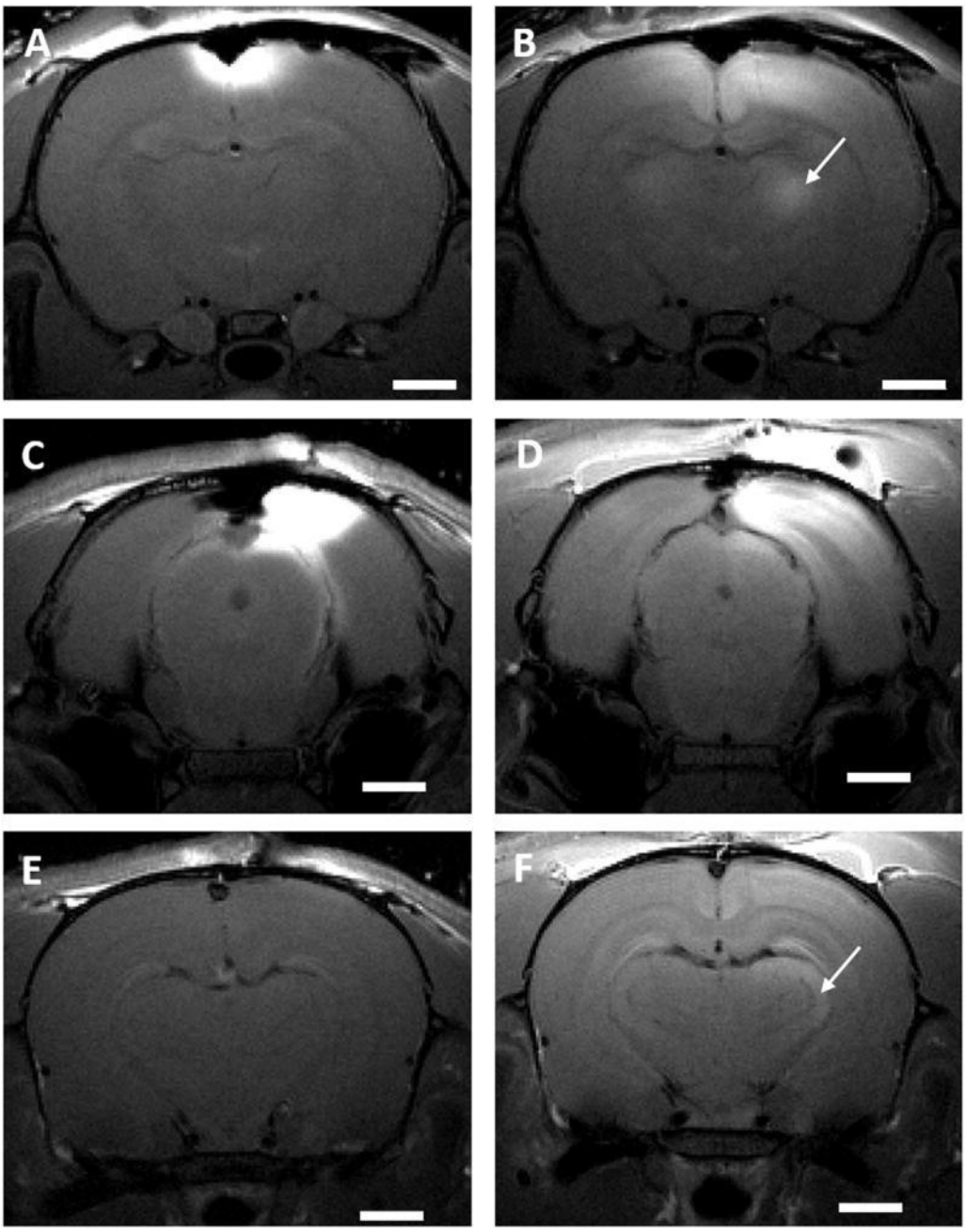

Figure 12. Transcranially delivered manganese.

(A). T_1-weighted images of rat brains that were administered 500 mM solution of $MnCl_2$ on the Bregma. Images were taken immediately after administration. (B). 24 hours after administration. (C). T_1-weighted images of rat brains that were administered 250mM solution of $MnCl_2$ and 250mM solution of $CaCl_2$ on the lambda. Images were taken immediately after administration. (D) 24 hours after administration. (E & F). Different slices from the same experiment as C and D. The scale bars are 2 mm.

One of the more popular investigated techniques for creative systemic manganese delivery has been through the use of subcutaneous osmotic pumps [53] [54] [55] [56]. Because of the toxicity when delivering manganese in high doses, these works have studied the effects of continuous delivery of low concentrations. Eschenko et al. showed that after a slow infusion over 7 days, there was an observable contrast within the brain [55]. Additionally, the slow infusion of manganese had no effect on the motor behavior in rats during voluntary wheel running. Mok et al. investigated the effects using the mini-osmotic pumps in the mouse model. They were able to produce results showing no observable toxic effects on animal physiology or behavior at significantly higher manganese doses than in previous studies [53]. Brand new work published in 2018 has continued the investigation of the use of implementing osmotic pumps. Vousden et al. used continuous delivery of manganese via osmotic pumps and investigated the time-course of signal enhancement and the effect of the continuous delivery on spatial learning and memory behavior [57]. They showed that spatial learning and memory based on the Morris Water Maze was not altered through $MnCl_2$ delivery. However, at high doses of osmotic infusion the mice developed adverse effects of skin ulcerations.

I will conclude this section by reiterating the diverse applications and uses that the manganese enhanced magnetic resonance imaging (MEMRI) technique can be applied to. This method can impact all facets of brain functional studies. In just this past year, MEMRI studies have been published in top journals investigating topics such as how microtubule-based axonal transport systems decline in Alzheimer's disease (AD) models [58], how remote sensorimotor stroke modifies the activity of hippocampal-thalamic networks [59], and how comprehensive developmental differences between male and female brains can contribute to our understanding of sex-specific tendencies in neuropsychiatric disorders [60].

1.9 Objective

I have described some of the major works in creative and new methods for delivering manganese to the brain for neuronal tract tracing studies. It is very important to find non-invasive methods that leave the brain intact, can be applied chronically, and can trace functionally activated pathways. Therefore, the main objectives of this thesis are as follows: 1.) use MEMRI to trace the projections of the vagus nerve to the brainstem, 2.) use VNS to alter the transportation of Mn^{2+}, and 3). Use MEMRI to trace the circuitry past the brainstem.

To address the first objective, a development of MRI-compatible rapid prototyping parts was conducted, extensive training in aseptic and surgical techniques was mastered, and a carefully planned imaging timeline was designed. I will present the design requirements and prototype iterations for improving image quality setup, show the results of improved image quality, reflect on the surgical techniques required for the experimental protocol, and discuss the importance of finding the correct image times for collecting data. To address the second objective, multiple sites of injections were investigated, along with the intervention method of VNS. I will show statistically significant, group-level maps of how VNS was able to alter the transport of Mn^{2+}. To address the third objective, possible second-order enhanced brain regions will be shown with an explored experimental validation. Additionally, consideration for future novel studies will be discussed and reflected on.

The overall potential of this work could lead to one day understanding how specific VNS parameters can activate specific functional pathways. For example, imagine using VNS parameters 'X' and observing Mn^{2+} from site A to B to C. Then, if the VNS parameters were changed to parameters 'Y', it might be possible to trace Mn^{2+} from site A to B to D. This potential could one day help give insight into the dependence of functionally activated brain pathways on VNS parameters.

2. METHODS AND DESIGN

2.1 Introduction

MEMRI experimental design includes lots of different factors to take into consideration. The concentration of Mn^{2+} must be optimized to minimize the adverse behavior effects and maximize region of interest tissue contrast. Additionally, one must maximize the resolution and plan out the necessary sequences for image collection. The researcher must also have an in-depth background with animal and surgical techniques to minimize experimental variability within groups and between groups. Within this chapter I will review the necessary steps for successful completion and repeatability of the vagal nerve tracing to the brain.

2.2 Experimental Design of Hardware

Imaging the nodose ganglion of the cervical vagus nerve and the brain stem of the rat can be challenging. A properly monitored, anesthetized rat has deep respiratory breaths throughout its torso that create movement along the neck and near the brain stem region. Because of the relatively long time it takes to sample an MR image, these breaths can create motion artifacts near the brainstem and other caudal regions. Furthermore, these motion artifacts can blur and distort features of the brain, which can lead to diagnosis mistakes. Therefore, one of the most important aspects of collecting high quality MR images for this application is minimizing motion artifacts. Typically, motion artifacts are minimized through the use of MRI compatible restraints or sequence addons such as respiratory gating. A gold standard device that has been used to minimize motion is the rat stereotaxic holder for benchtop brain studies. This device uses three points of contact with a rodent's head in order to minimize motion during brain surgeries and electrode recordings. The stereotaxic rodent head holder is not MRI compatible, so I used many of its components for inspiration when designing a custom device. Here, I will outline the experimental goals, requirements, design procedure, and prototype iterations when designing the custom head holder used for data collection.

2.2.1 Hardware Design Requirements

The design requirements for the different subcomponents of the assembly are shown in Tables 1-4. The subcomponents are listed as the head holder, the nose cone, the bite bar, and the ear bar. Each table shows the specific descriptions of the requirements, along with the priority level for design. Five is the highest priority and one is the lowest priority. Some examples of high priority design requirements that were used for the assembly include MRI compatibility, having specific dimensions to ensure the assembly pieces fit together and do not vibrate, and making sure the subcomponents are durable. A couple examples of low priority design requirements were making sure the head holder was visually aesthetic and having easy assembly. These low priority requirements were given low priority scores because they did not relate directly to improving image quality or aid in rodent comfort.

Table 1. Design requirements of the head holder.

Req. Number	Description	Priority (1-5)	Subcomponent
1	Able to connect to the body holder	4	Head Holder
2	Supports rodents of various sizes (100g – 800g)	5	Head Holder
3	Allows for easy assembly with the nose cone, bite bar, and ear bars	3	Head Holder
5	Correct design dimensions to fit the ear bars	5	Head Holder
6	Correct design dimensions to fit the bite bar	5	Head Holder
7	Aesthetic visual design	2	Head Holder
8	MRI compatible	5	Head Holder
9	Able to be machined to include threading for thumb screws and plastic pins for the surface coil	5	Head Holder

Table 2. Design requirements of the nose cone.

Req. Number	Description	Priority (1-5)	Subcomponent
1	Allows for easy assembly with the head holder	3	Nose Cone
2	Correct design dimensions to fit the bite bar	5	Nose Cone
3	Correct design dimensions for the anesthetic tubing	5	Nose Cone
4	MRI compatible	5	Nose Cone

Table 3. Design requirements of the bite bar.

Req. Number	Description	Priority (1-5)	Subcomponent
1	Correct design dimensions to fit through the head holder and bite bar, simultaneously	5	Bite Bar
2	Strong enough to keep the head of the rodent stable during anesthetization, no bending	5	Bite Bar
3	Correct design dimensions for a range of sizes of rodent teeth to fit through the hole	4	Bite Bar
4	MRI compatible	5	Bite Bar

Table 4. Design requirements of the ear bars.

Req. Number	Description	Priority (1-5)	Subcomponent
1	Correct design dimensions to fit through the head holder	5	Ear Bar
2	Strong enough to keep the head of the rodent stable during anesthetization, no bending	5	Ear Bar
3	Correct design dimensions for a range of sizes of rodent heads	4	Ear Bar
4	Dull enough to ensure that the rodent is not in pain during fixation	5	Ear Bar
5	MRI compatible	5	Ear Bar

2.2.2 Design and Prototype Iterations

The 3D design was completed in the design software Autodesk Inventor 2015. All of the different subcomponents were designed as .ipt files, dimensioned out and annotated specifically into .idw files, and then were submitted for rapid prototyping as .stl files. Figure 13 shows the annotated and dimensioned out drawing files of the head holder and nose cone, respectively.

The head holder was the main subcomponent of the assembly. This was the piece that attaches to the current, MRI, cantilever system and body holder. It was the main structural piece and needed to be able to fit snug with all parts. The nose cone was where the nose of the rat fit into in order to continuously deliver anesthetic. This piece had three different hole openings: an input hole for the anesthetic tubing, an output hole for the anesthetic tubing, and a hole that the bite bar fit through. The ear bar and bite bar were smaller parts that were used to minimize motion of the skull. Simply put, one ear bar went into each ear of the rat, and the bite bar

supported the teeth of the rat. This fixated the skull at three points of contact in order to optimize MR image quality.

After the head holder and the nose cone were rapid prototyped, they were post-processed within a machine shop. Both of these parts were printed with ABS M30 material. This material allowed for easy post-processing and was MRI compatible. The post-processing included small sanding to the bottom and sides of the nose cone in order to ensure that it fit perfectly into the head holder. Additionally, the head holder holes were threaded with taps. The threading allowed for specific thumb screws to screw into the holder, which was necessary for surface coil attachment and fastening. Specifically, 16 of the holes that ran along the upper surface were threaded with size M3 by 0.5, and 9 of the holes were threaded with size M4 by 0.7.

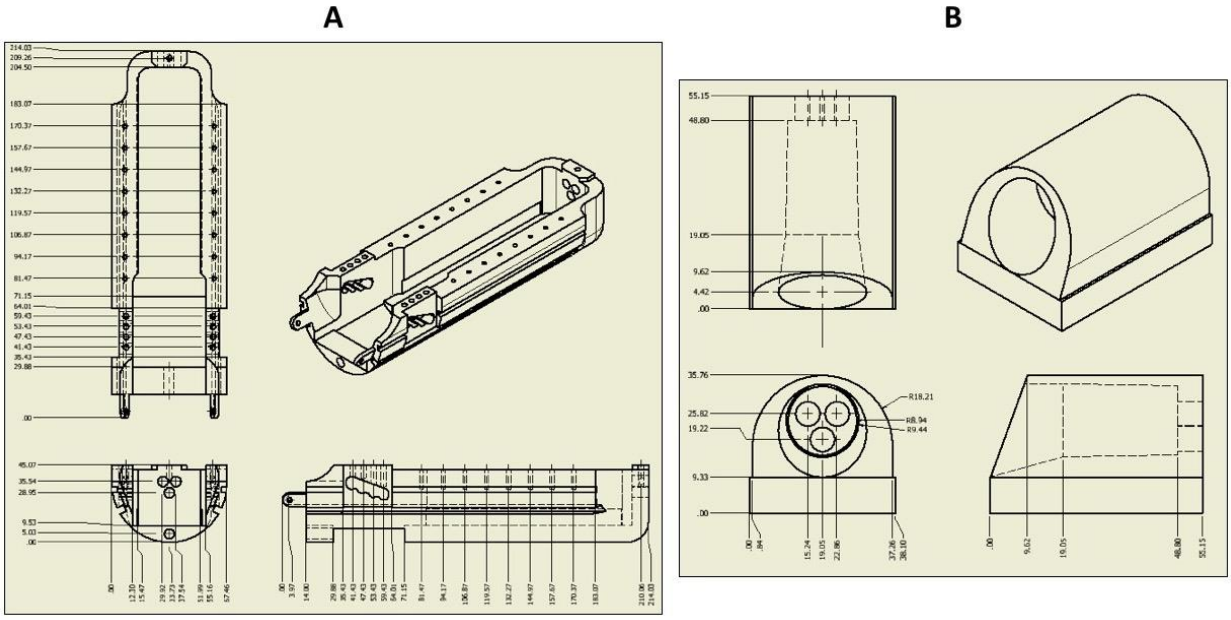

Figure 13. Annotated drawing layouts for the design process of the holder assembly. (A). This was the full view representation of the animal holder design. (B). This was the full view representation of the nose cone design. Note that all dimensions are in millimeters (mm).

The bite bar and ear bars were machine shopped from cylindrical rod stock made from PEEK. These are shown in Figure 14 below. PEEK is an MRI compatible material that has excellent tensile strength (14,000 psi), which is often used as a lightweight substitute for metal parts in high-temperature, high-stress applications. It also resists chemicals, wear, and moisture. As can be seen in the figure demonstrating the designs, the initial bite bars that were made from

ABS M30 material were not durable enough and resulted in breaks. The far-left prototype design had a completely broken end. Therefore, the PEEK material proved to be great for multiple uses. The skinnier PEEK bite bar (third from the left) was the final design.

The fully manufactured and assembly design is shown below in Figure 15. The entire head holder assembly fastened into the white body holder, which was then cantilevered into the bore of the magnet during an MRI session. As can be seen, the bite bar aligned through the back of the head holder and the nose cone. Additionally, the back of the head holder had a thumb screw that could be used to tighten the position of the bite bar. The anesthetic tube connections were not shown. The ear bars could also be seen on both sides of the head holder. Panel C of Figure 15 showed what the setup looked like when the volume coil was attached to the assembly.

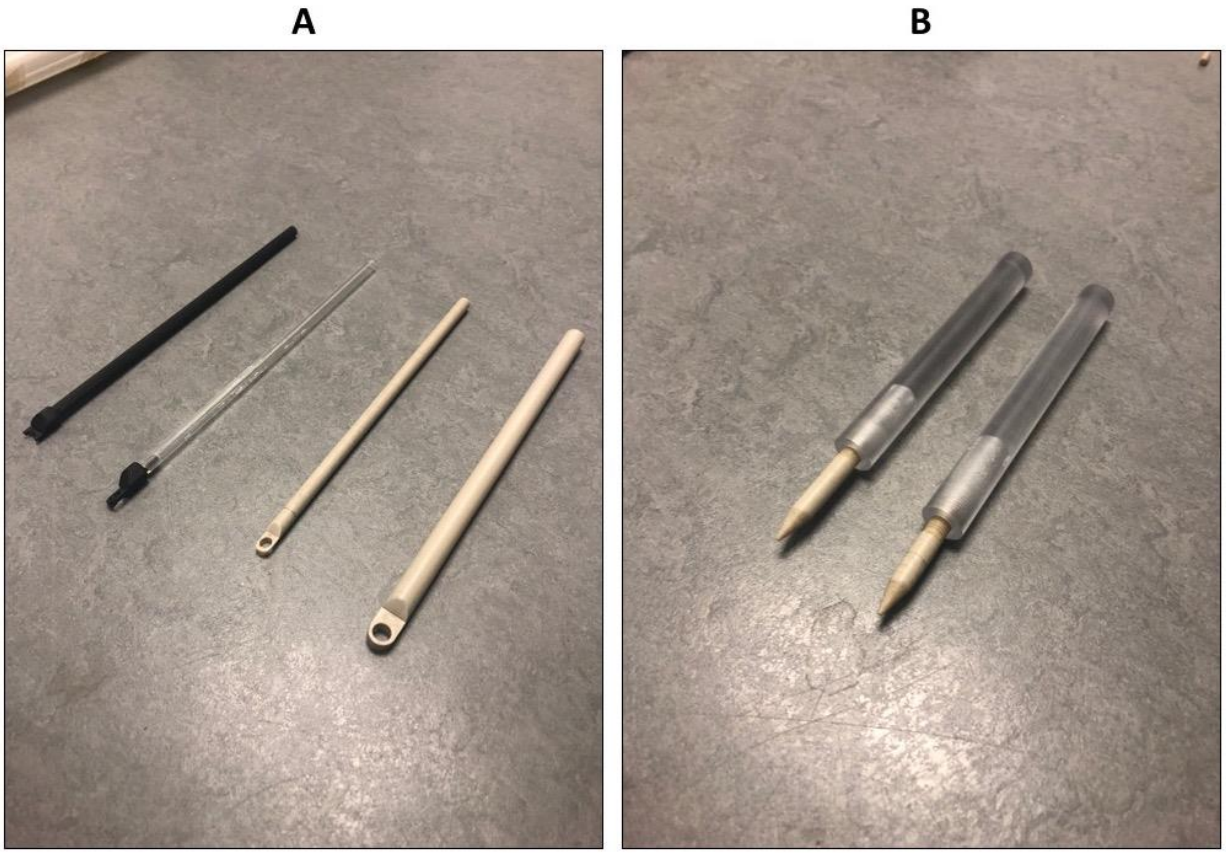

Figure 14. Bite bar iterations and ear bars used within the MEMRI experiment.

(A). The iterations for the bite bars are shown here. The design on the far left was manufactured with rapid prototyping from ABS M30 material. The design second to the left was made from a transparent plastic rod and used a rapid prototyped end made from ABS M30. The two designs on the right were manufactured within a machine shop from PEEK rod material. (B). The ear

bars are specifically the end pieces that are shown screwed into the transparent, plastic handles. The ear bars were manufactured within a machine shop from PEEK rod material.

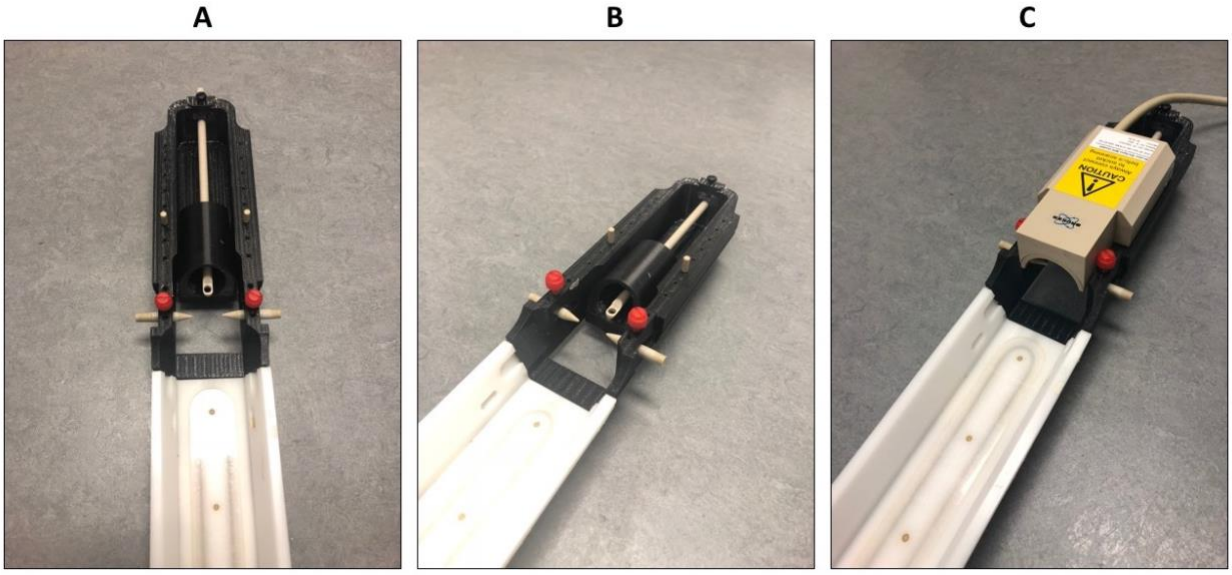

Figure 15. Full assembly view of all the attached design subcomponents.

(A). Full assembly front view of the animal restraint design. Note that the white structure is the body holder, which was not designed in-house. (B). Full assembly isometric view of the animal restraint design. (C). Full assembly isometric view of the animal restraint design that demonstrated how the surface coil attached onto the body holder. Specifically, the surface coil fits over the two, tan, plastic pins that were screwed into the top of the holder. These pins can be seen in panels A and B.

After the full holder design was engineered, the assembly design was used for functional MRI (fMRI) experiments. Part of post-processing for fMRI experiments, was a motion correction technique that quantified the amount of head displacement in the superior, left, and posterior directions. Figure 16 and 17 the results of the motion trace for the head displacement. Specifically, Figure 16 shows results of fMRI experiments that used a commercial head holder, and Figure 17 shows results of fMRI experiments that used the new, custom head holder. As can be seen, the commercial body holder had increased displacement over time in the superior direction, whereas the custom holder minimized all motion.

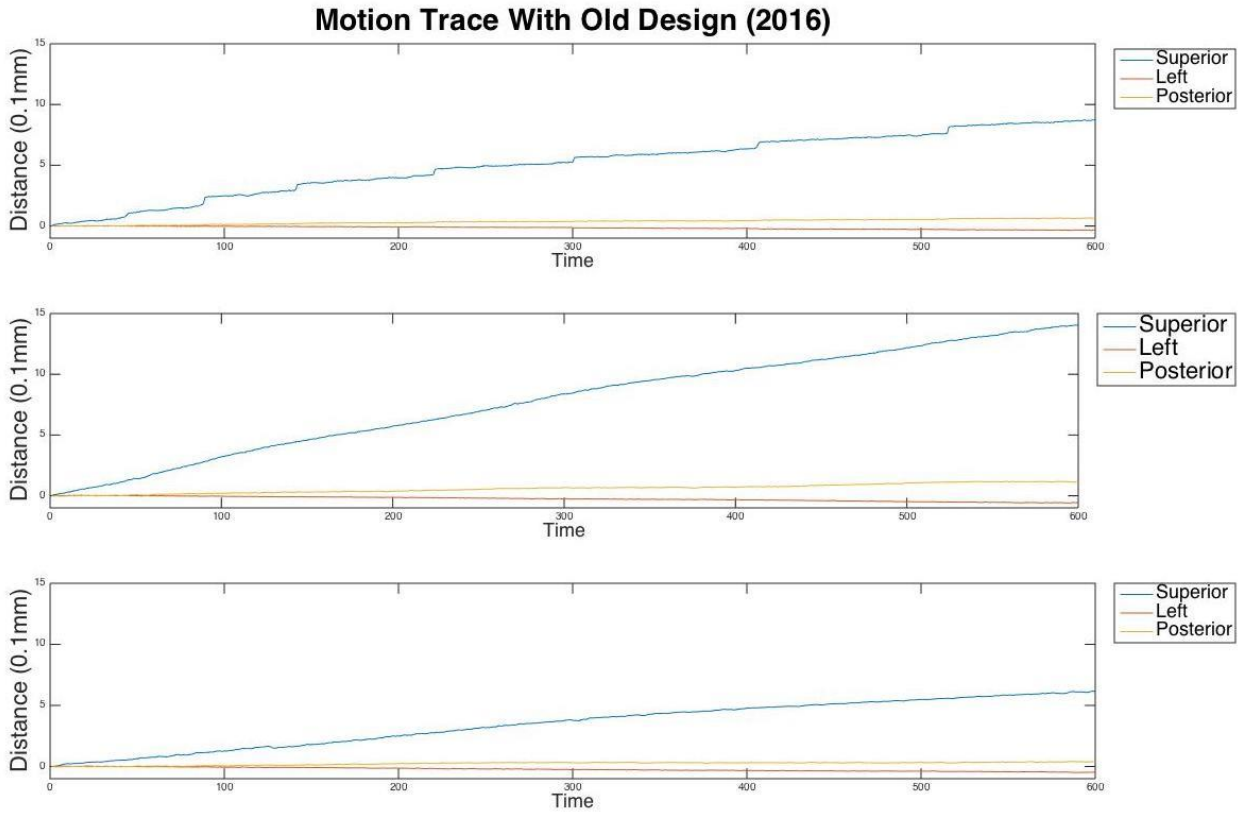

Figure 16. Motion trace of the old head displacement.

Three different fMRI experiments completed in 2016 using a commercial head holder. Notice the increased displacement in the superior direction over time.

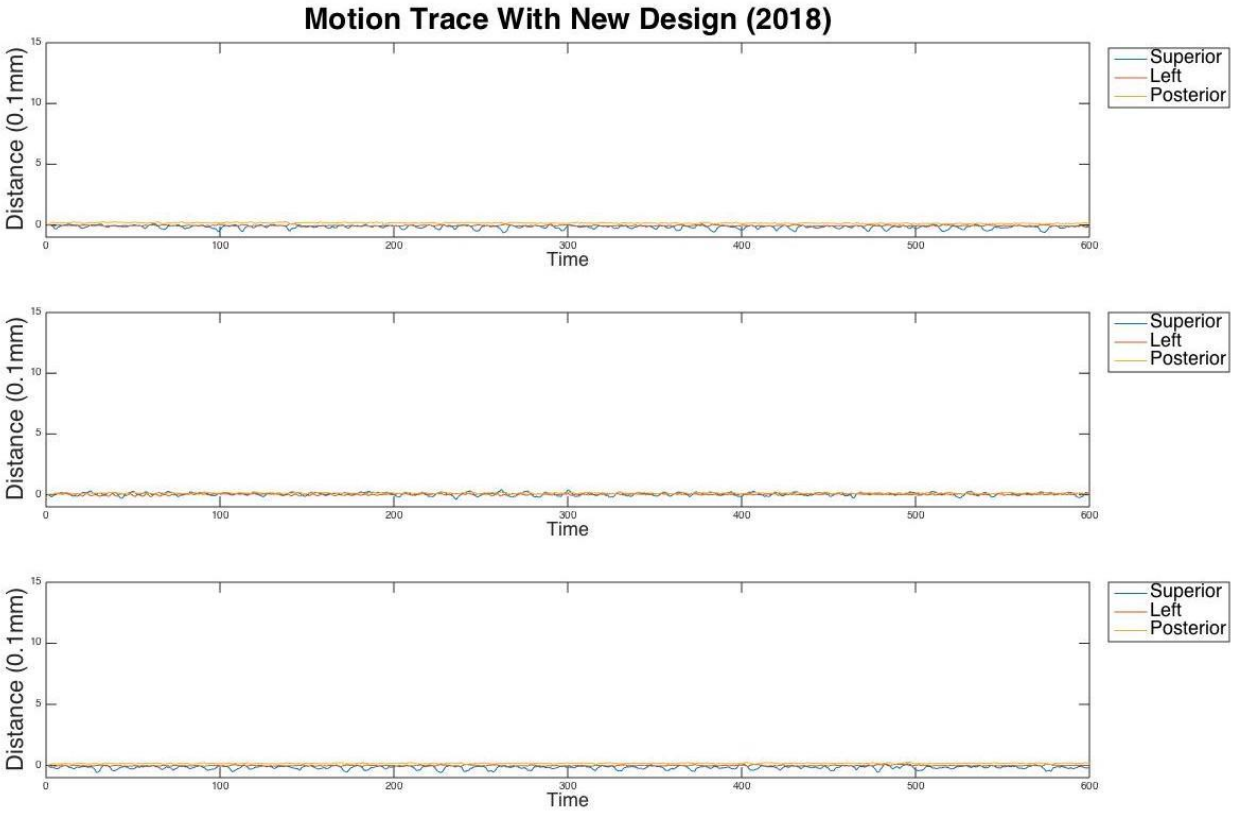

Figure 17. Motion trace of the new head displacement.

Three different fMRI experiments completed in 2018 using the custom head holder. Notice the motion displacement was minimized in all directions.

2.3 Rodent Handling and Surgical Technique

The results that will be demonstrated throughout this thesis rely heavily on proper knowledge and training related to experimental rodent procedures and surgeries. It is vital that the correct training has been completed before attempting such experiments. This is to ensure that the rat model subjects are monitored correctly and do not experience any adverse effects related to the study. All protocol details were approved by Purdue's Animal Care and Use Committee (PACUC).

2.3.1 Rodent Training

Here, I will list the specific trainings that I completed prior to any rodent handling or research collection. The on-line training procedure modules that were completed before working with rodent models were as follows: animal biosafety, working with Institutional Animal Care

and Use Committee (IACUC), principal investigators and Institutional Biosafety Committee (IBC) members, working with mice, and working with rats.

The in-person, rodent training procedures that were completed prior to experimental data collection include the following: basic handling/restraint and gender determination, basic injections, tail vein injections, euthanasia, basic necropsy, cardiac blood collection, cervical dislocation, basic suturing and wound closure, oral gavage, and aseptic techniques.

2.3.2 Surgical and MRI Protocol Specifics

All rats were weighed and anesthetized under 5% isoflurane (500 mL/min) for five minutes. Anesthetization was maintained throughout MR scanning at a determined anesthetization level (500mL/min, 1%-3% anesthesia level) depending on the rats' monitored physiological vitals. Specifically, respiratory rate (40-60 bpm) and temperature (37°C) were monitored and controlled during imaging. The rats were placed prone in a custom rat holder that was designed as previously described. The rats' noses were positioned in a nose cone. Motion was minimized through the use of the custom manufactured bite bar and ear bars. A surface coil was placed on top of the head and fastened down before the animal was scanned in a 7T small-animal MRI system (BioSpec 70/30, Bruker). A 2D, T_2 Turbo RARE sequences with no gaps was used to obtain T_2-weighted brainstem images. Also, a 3D, T_1 RARE sequences with no gaps was used to obtain T_1-weighted brainstem images. These sequences were prescribed the same. After this baseline imaging session, the rats were moved to a nearby surgical station and underwent surgery.

Before the surgery, the surgical area was cleaned with iodine to reduce bacterial contamination, and the rats were given an injection of carprofen to reduce pain and inflammatory effects. The rats were laid supine and were cut open along their neck in order to visualize the left or right carotid artery. From there, the specific side of the cervical vagus nerve ran parallel to the carotid artery, and the nodose ganglion could be located. After the nodose ganglion was located, the rats were microinjected with 1.0µl of 500mM $MnCl_2$ and were implanted with a biphasic electrode. The microinjection used a Nanofil 10µl sub-microliter injection system (World Precision Instruments, Sarasota, FL) with a beveled 35g needle. The $MnCl_2$ solution was mixed with a blue dye, which makes it easy to visually determine if the injection was successful. The first group (n=5) was injected in the left nodose ganglion and was stimulated along the left

cervical vagus nerve for four hours with electrical pulses from previous preclinical studies. The second group (n=9) was injected in the left nodose ganglion, implanted along the left cervical vagus nerve, but was not stimulated. The third group (n=5) was injected in the right nodose ganglion, implanted along the right cervical vagus nerve, and was also not stimulated. It was important to note that even if the rodent was not receiving vagus nerve stimulation, all rats were implanted with the electrode in order to ensure that similar nerve manipulation was experienced by all rats. The first group was allowed to recover from surgery after the stimulation period, whereas the other two groups began their recovery after their injections. All rodents were sutured up with discontinuous sutures along the entire opening to ensure that the opening was not able be tampered with. Furthermore, all three groups of rats were imaged at the same post-injection times to accurately compare Mn^{2+} transport.

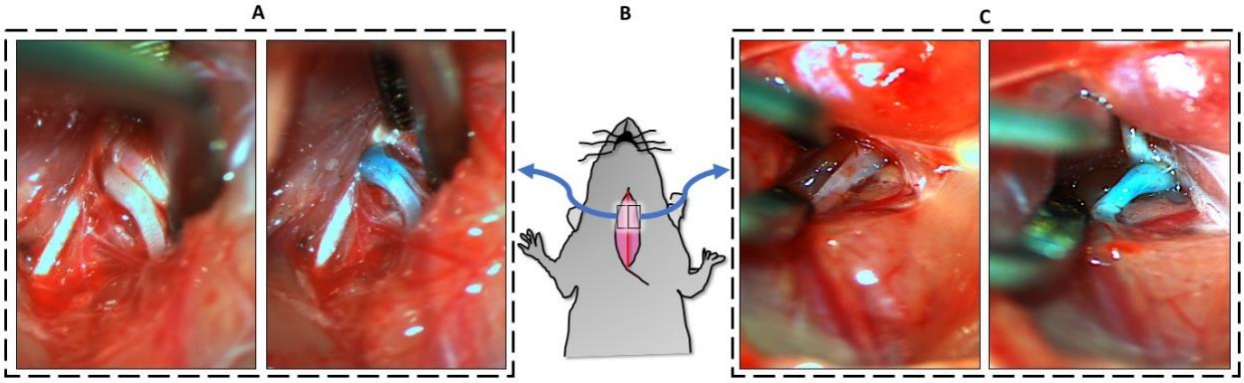

Figure 18. Surgical injection of $MnCl_2$ into the specific nodose ganglion.

(A). These panels demonstrated the before and after photos of an injection into the right nodose ganglion. Before injection, the nodose ganglion is the white bulb in the left image. After injection, the blue $MnCl_2$ solution was clearly visible inside of the right nodose ganglion. (B). This shows a drawing of a rat laying supine during surgery. The rat is opened in order to implant a biphasic electrode and complete a microinjection. (C). These images demonstrated the before and after photos of an injection into the left nodose ganglion. Again, before injection, the nodose ganglion is a white bulb. After injection, the blue $MnCl_2$ solution was clearly visible inside of the left nodose.

2.4 Stimulation Parameters

The group that received VNS was stimulated for four hours with electrical pulses from previous preclinical studies. The parameters are as follows: biphasic square pulses with inter-

pulse duration (IPD) = 50ms; pulse amplitude (PA) = 1mA; pulse width (PW) = 0.5ms; frequency = 5Hz; 20 seconds on and 40 seconds off.

2.5 Experimental Timeline

Planning out a detailed timeline for imaging throughout manganese tracing is important. One of the benefits of MEMRI is that the rat is able to act in an awake, and freely behaving environment. Therefore, the brain activity of the rodent was continually reflected in the transportation of the manganese, which can be sampled at specific times. Additionally, it is important to take into consideration the effect that anesthetics have on the transport of manganese.

First, it was important to determine the feasibility of tracing 500mM $MnCl_2$ to the NTS region of the brainstem, which is the first known anatomical site within the vagal nerve projection. For this feasibility check I completed the previously described surgical protocol. The specific injection site was the left nodose ganglion, and the rats did not receive VNS. At 24 hours post-injection, the rats (n=3) were sacrificed and imaged again in order to observe where the manganese had accumulated and transported to. It is important to note that a control group (n=3) was also investigated, which consisted of injections of gadolinium into the nodose ganglion instead of $MnCl_2$. Gadolinium (Gd) is another paramagnetic contrast agent. However, it is not a calcium analogue. Therefore, it is theoretically not able to enter excitable cells by transport through calcium channels, and unable to transport along axons into the brain. By comparing the $MnCl_2$ injected results with the Gd injected results, I was able to answer the following question: Is Mn^{2+} transport from the nodose ganglion to the brain stem feasible and neuronal?

Next, I wanted to investigate if there were specific, second-order regions of the brain that the manganese transported to. Therefore, I conducted post-injection imaging at more post-injection times, and over a longer period of time. Specifically, I imaged a group of rats (n=3) at baseline, 12 hours post-injection, 24 hours post-injection, and 48 hours post-injection. This would allow me to determine the peak accumulation time of manganese within the NTS, and any repeatable second-order transport brain regions.

Finally, I planned out specific experimental groups. As stated in the experimental protocol, the groups are as follows:

- The first group (n=5) was injected with 1.0µl of 500mM $MnCl_2$ in the left nodose ganglion and was stimulated along the left cervical vagus nerve for four hours with electrical pulses.
- The second group (n=9) was injected with 1.0µl of 500mM $MnCl_2$ in the left nodose ganglion, implanted with the electrode along the left cervical vagus nerve, but not stimulated.
- The third group (n=5) was injected with 1.0µl of 500mM $MnCl_2$ in the right nodose ganglion, implanted along the right cervical vagus nerve, and was also not stimulated.

The Figure 19 below shows the specific experimental timelines for the three different experimental groups. All of the rats in these three groups were imaged at baseline, 12 hours post-injection, and 24 hours post-injection. By comparing these experimental groups I was able to answer three experimental questions:

1. Are Mn^{2+} enhancement patters dependent on the injection site? ($MnCl_2$ left nodose injected results vs. $MnCl_2$ right injected results)
2. Dose VNS promote the transport of Mn^{2+}? ($MnCl_2$ left nodose injected results vs. $MnCl_2$ left injected results with VNS)
3. Does VNS change the brain region of Mn^{2+} accumulation? ($MnCl_2$ left nodose injected results vs. $MnCl_2$ left injected results with VNS)

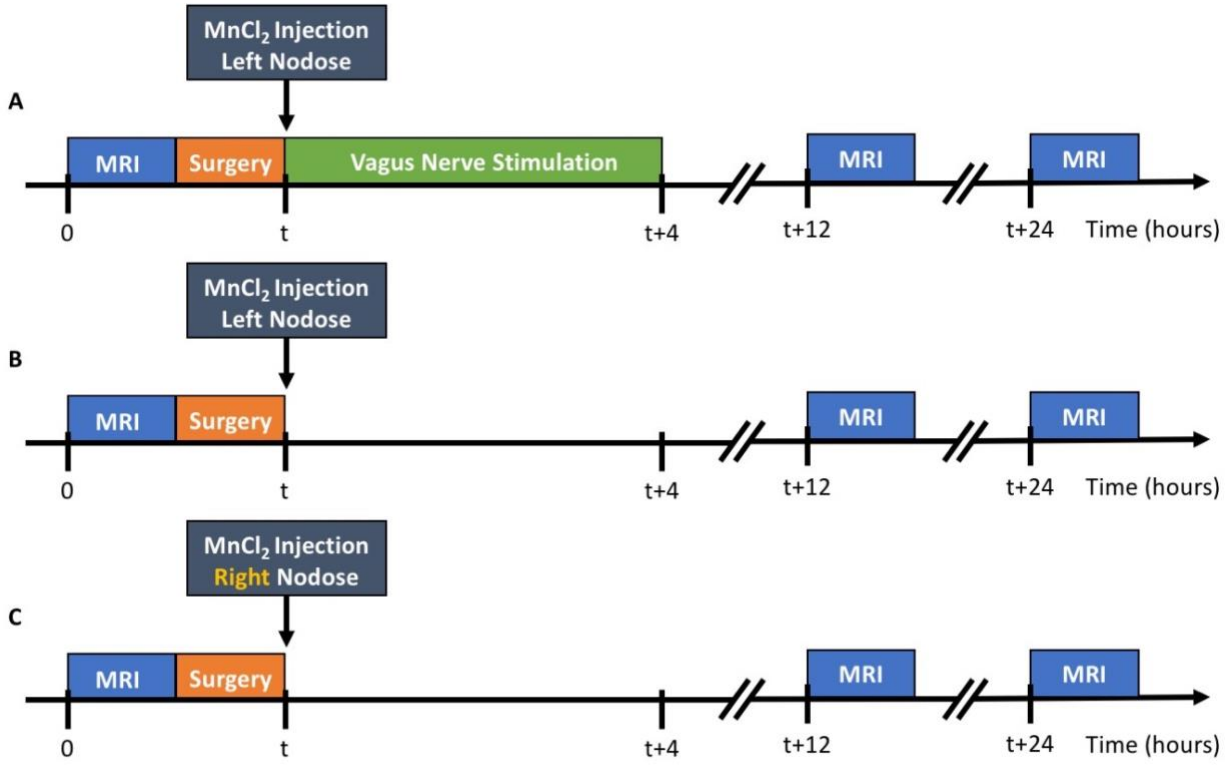

Figure 19. Paradigm for the three different experimental rodent groups.

(A). The timeline for the first experimental group. The site of injection was the left nodose ganglion, and the subjects underwent vagus nerve stimulation immediately after injection. (B). The timeline for the second experimental group. The site of injection was the left nodose ganglion, but the subjects in this group did not undergo VNS. (C). The timeline for the third experimental group. The site of injection was the right nodose ganglion, and the subjects in this group did not undergo VNS.

2.6 MRI Sequences

The MRI sequences that were used for this thesis consisted of the following: a one slice localizer, a multi-slice localizer to determine region of interest, a 2D T_2 Turbo RARE sequence, and a 3D T_1 RARE sequence. Specifically, the 2D, T_2 Turbo RARE sequence had no gaps and was used to obtain T_2-weighted brainstem images (TR/TE = 6637.715/32.50ms; FA = 90°; matrix size = 192 x 192; FOV = 32 x 32mm; slice thickness = 0.438mm; slices = 64; averages = 2). The 3D, T_1 RARE sequence also had no gaps and was used to obtain T_1-weighted brainstem images (TR/TE = 300/10ms; FA = 90°; matrix size = 192 x 192 x 64; FOV = 32 x 32mm x 28mm; four averages). The T_2-weighted sequence was prescribed by locating the anterior and

posterior commissures from the multi-slice localizer, and the T_1-weighted sequence was then prescribed at the same location and geometry.

2.7 Anatomical MRI Features

The images that were acquired for this protocol were T_2-weighted and T_1-weighted. The following figure shows sample T_2-weighted images and T_1-weighted images that were collected during a baseline scan. It is important to understand where specific landmarks are within these images because they were expected sites of enhancement during post-injection scans. These landmarks were all part of the vagus nerve projection to the solitary tract nucleus (NTS). The landmarks that are shown were chosen from Paxinos and Watson's rat brain atlas [61]. Specifically, the anatomy was referenced between regions of Bregma -14.40 mm and Bregman -13.92 mm. The full names of the anatomical landmark abbreviations can be referenced within the index of anatomical abbreviations.

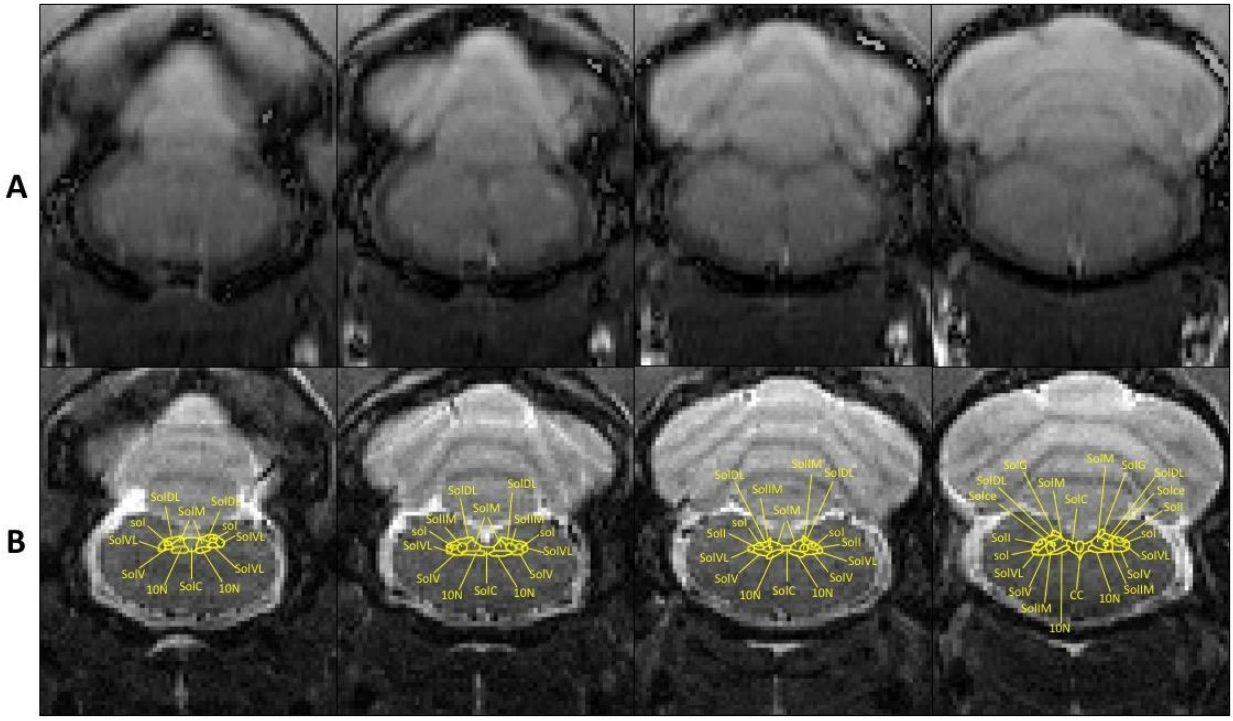

Figure 20. Demonstration of T_1-weighted and T_2-weighted images showing the different anatomical landmarks of the NTS within the brainstem.

(A). This row of brainstem images were the T_1-weighted MR images at baseline of a sample rodent. The left most image was the most caudal, and as the images progressed towards the right, the location was further rostral. (B). This row of brainstem images were the corresponding T_2-weighted MR images at baseline of the same rodent. The images progressed from caudal to rostral, from left to right. Additionally, anatomical regions of the NTS were manually drawn on the slices and labeled according to Paxinos and Watson's *The Rat Brain in Stereotaxis Coordinates Seventh Edition*.

2.8 MRI Analysis

MRI data was pre-processed using FSL [62] and AFNI [63] to visualize the statistically significant enhancement at a group-level. To do this, all MRI images were reoriented using MATLAB and the 3dresample function from AFNI in order to change their axis order. The template was resampled to the same dimensions as the T_2-weighted anatomical images, and then the T_2-weighted images were linearly registered to the MNI brain template using FLIRT and the finesearch option. Specifically, FLIRT performs affine registration, which is generated by a calculated affine transformation from an input and reference volume. The T_1-weighted brain images were then preprocessed. First, the T_1-weighted images had their axis reordered using AFNI. Next, the T_2-weighted images were resampled to the same resolution as the T_1-weighted

images, which was also completed using AFNI. The T_1-weighted images were then linearly registered to the T_2-weighted images using FLIRT and the finesearch option. Next, the template was resampled to the same resolution as the T_1-weighted images, and the resampled T_2-weighted images were linearly aligned to the template. Finally, the T_1-weighted images were warped to the MNI space using FLIRT based on the linear relationship between the T_2-weighted data and template data. The brain was also extracted within the MNI space from the rest of the head and saved as a new volume for analysis.

All images were normalized by the average signal intensity within the brain for each slice. For post-injection images, this assumed that the number of brain voxels enhanced by the manganese in each slice was specific, and that there was minimal leakage from the injection. Therefore, the enhancement caused by manganese would not significantly alter the normalization of the signal intensity. This normalization was completed to account for the effects of B_1 inhomogeneity.

Finally, the post-injection normalized signal intensity increases were calculated and quantified relative to the pre-injection images using a custom MATLAB script. In order to calculate the differences, the normalized signal intensity in each baseline brain voxel was subtracted from the normalized signal intensity in the linearly aligned post-injection voxel, and then that difference was divided by the normalized signal intensity from the baseline voxel. This is equal to the percent change in T_1-weighted normalized signal intensity and was used to generate percent signal enhancement maps. Next, statistics were calculated in order to determine the significant areas of enhancement. For each rat, a one-tailed (right) paired t-test was calculated for every voxel at a confidence level of 98% (alpha = 0.02). The one-tailed, paired t-test compared the normalized signal intensity at baseline and the different post-injection times to determine if there was a significant increase in normalized signal intensity. The statistically significant voxels could then be mapped at a group-level, which were expressed as the percent increase in the T_1-weighted normalized signal intensity. This statistical analysis approach was completed for each experimental group.

The programs 3D Slicer and FSLView were used to for 3D visualizations.

2.9 Timms Silver Sulphide Protocol

Immediately after post-injection MR imaging, rats (n=6) were moved to Dr. Terry Powley's lab for the beginning of the Timms Sulphide Silver staining procedure. This staining method is used to visualize metals in the brain like manganese. Specifically, two rats were transported after 24 hours post-injection imaging, two rats were transported after 12 hours post-injection imaging, and two rats were transported as controls, which had not undergone injections.

All rats were given an overdose IP injection of Ketamine/Xylazine, and then were perfused through their heart with 1x PBS at 25 ml/min for 10 min (total volume = 250ml). Next, the perfusion was switched to sulfide perfusate and perfused for 20 min (total volume = 500ml). The brains were removed and placed into sulfide perfusate solution for 40 min on a shaker table. The brains were rinsed with deionized water and transferred to 10% neutral buffered formalin overnight on a shaker table in a refrigerator. On day 2 of the protocol, the brains were transferred to glutaraldehyde solution for 1.5 hours on a shaker table, and then returned to 10% neutral buffered formalin for 24 hours on a shaker table in a refrigerator. On day 3 of the protocol, the brains were transferred to 70% EtOH for 4 hours minimum. The brains were allowed to remain in 70% EtOH for multiple days if needed. They were then transferred for histology and paraffin embedding. On day 4, a small scoop of gelatin and a small amount of chromium potassium sulfate was added to the water bath and allowed to dissolve. The water bath was heated to 45 degrees Celsius. The medulla was sectioned at 10μm and mounted on positively charged slides, which were dried in an oven overnight at 60 degrees Celsius. On day 5, staining jars and cylinders were prepared by being washed with nitric acid. Deparaffinized slides were washed in xylene 3 times for 3 minutes each, 2 times for 3 minutes each in 100% EtOH, 2 times for 3 minutes each in 95% EtOH, 1 time for 3 minutes in 70% EtOH, and 2 times for 3 minutes each in distilled H2O. The slides were placed in nitric acid washed coplin jars. The coplin jars had lids in order to minimize light penetration. Additionally, plastic forceps were used when transferring slides for this stain. The sections were stained in preheated Timms solution at 26 degrees Celsius for 30 minutes in the dark and then placed on a shaker table during staining. After, they were transferred to 60 degrees Celsius Timms stain solution for 10 min in the dark and placed in a circulating water bath set to 60 degrees Celsius. The stained slides were rinsed in two changes of water for 3 minutes each and then ran through 1 min in 70% EtOH, 2 washes of 1 min in 95%

EtOH, 2 washes for 2 min in 100% EtOH, and 3 washes for 4 min in xylene. The slides were finally covered with Cytoseal. The solutions were created as described here:

- Sulfide Perfusate: 2.9g Sodium sulfide nonahydrate, 3.0g Sodium phosphate monobasic, and 250ml ultrapure H_2O
- Glutaraldehyde Post-fix: 10ml 25% Glutaraldehyde, 24g Dextrose, and 70ml ultrapure H_2O
- Timms Stain Solution: mix 120ml Gum Arabic with 20ml Citrate buffer and 60ml Hydroquinone, heat to 26 degrees Celsius, and 1ml of 1M Silver nitrate
- Gum Arabic: 500g gum Arabic, 1000ml dissolved for 3-4 days, and then aliquoted into 50ml tubes and frozen at -20 degrees Celsius
- Citrate Buffer: 5.1g Citric acid and 4.7g Sodium citrate to 20ml ultrapure water
- Hydroquinone Developer: 3.4g hydroquinone to 60ml ultrapure H_2O

2.10 Microscopy Image Acquisition and Analysis

The images were acquired using a Leica DMRE microscope, with a "SPOT Imaging" camera and software system. All images were shot using a 10x objective lens. Additionally, Photoshop was used to adjust the contrast and brightness. The scale bars were applied by referencing a photo containing a ruler photographed at 10x. The scale bars were 250μm. Some of the images were also rotate and cropped to ensure consistent presentation of the region of interest.

3. NEURONAL TRACT TRACING PATTERNS

3.1 Outline of Investigation

I will present data that investigated the feasibility of manganese transport from the periphery into the central nervous system. This will include comparison of $MnCl_2$ injected results to Gd injected (control) results in order to verify feasibility. Additionally, I will show data that explores second-order transport by increasing the time between injection and the final post-injection imaging session. Finally, I will show sample single subject data for the different experimental groups, group-level data for the different groups, and compare the results on a group level. In MEMRI studies it is important to show both single subject and group-level data to confirm visual enhancement and accumulation of manganese. This helped demonstrate an optimized concentration of manganese for clear tissue contrast.

3.2 Early Investigation of Manganese Transport

The beginning of this investigation was started by exploring post-injection results of manganese injected rats. The figures in this section show the brainstem slices of the rat at baseline (pre-injection) and at 24 hours post-injection after an injection of 1.0µl of 500mM $MnCl_2$ into the left nodose ganglion. As can be seen, enhancement of the left nodose ganglion is labeled with a green arrow, enhancement of the vagus fiber tract is labeled with a red arrow, enhancement of the left NTS is shown with a yellow arrow, and enhancement of the right NTS is pointed to with an orange arrow. The orange arrow pointed out a particularly exciting site of enhancement because the right NTS is contralateral to the left nodose ganglion. This means the manganese was injected into the left nodose ganglion, transported along the vagus nerve into the brain stem, accumulated within the left NTS, and was postsynaptically taken up by the right NTS. This is clear evidence that the manganese was able to transport across a synapse. This subject was sacrificed before the 24 hours post-injection MR imaging in order to minimize all motion and allow for clear observation of all enhancement. Because the rat was sacrificed, I was not able to image at later times to observe possible further transport of the manganese. The rest of the brain slices were also visually inspected for enhancement, but enhancement in other brain regions was not observed.

The results also supported the use of the relatively large dose of manganese in this study. Specifically, the dose of manganese was not toxic enough to notice stress, or abnormal visual appearances like porphyrin around the eyes and nose, or piloerection [64]. Piloerection is a symptom of stress, shown as a rough coat of fur. Additionally, the results proved that the manganese dose was high enough to observe clear tissue contrast within the site of injection, along the fiber tract, and within the first site of accumulation. This was observed visually.

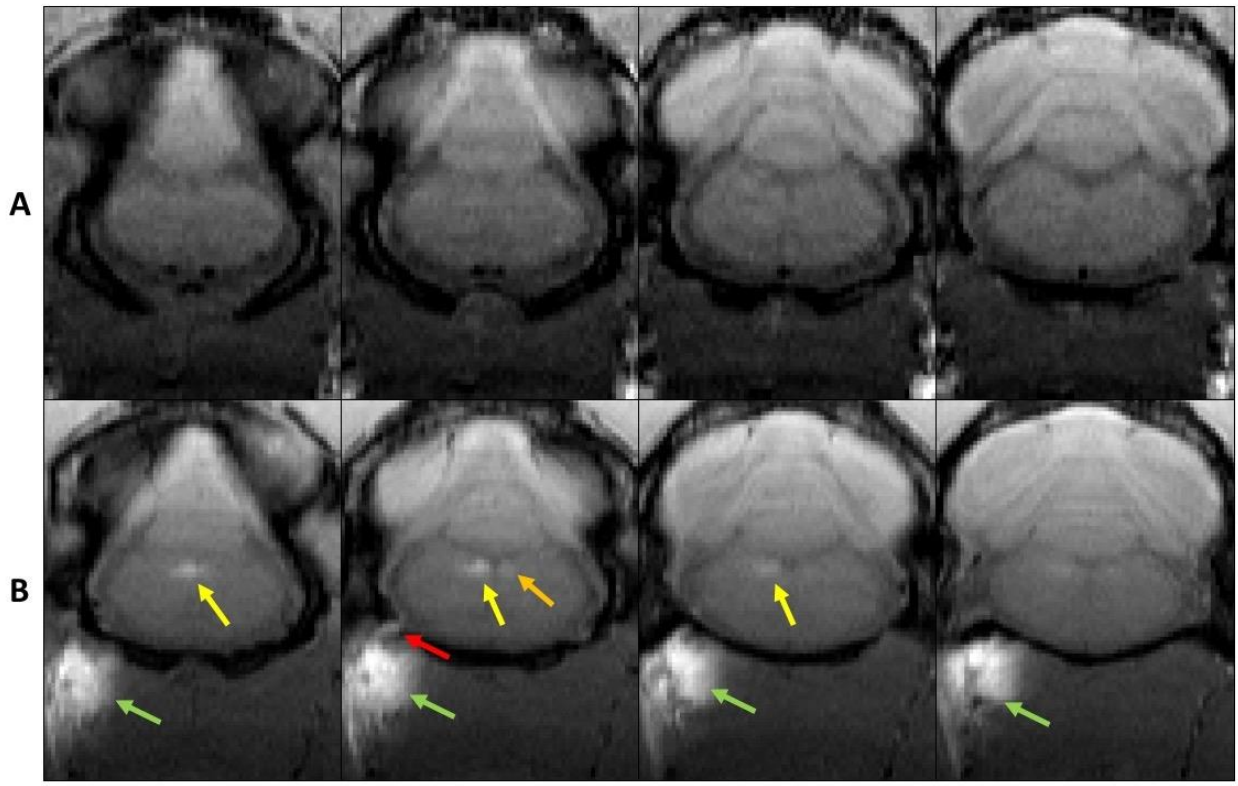

Figure 21. Single subject comparison of baseline and 24 hours post-injection manganese transport.

(A). This row of brainstem images were the T_1-weighted MR images at baseline. The left most image was the most caudal, and as the images progressed towards the right, the location was further rostral. (B). This row of brainstem images consisted of the T_1-weighted MR images at 24 hours post-injection of 1.0µl of 500mM $MnCl_2$ into the left nodose ganglion. The images were manually matched to the baseline images and also progressed from caudal to rostral, from left to right. Notice the positive enhancement within the nodose ganglion (green arrow), along the fiber tract (red arrow), large enhancement in the left NTS (yellow arrow), and small enhancement in the right NTS (orange arrow).

Although it was observed that the manganese was able to transport along the vagus nerve and transport across a synapse, the experiment needed a control in order to verify the results. Thus, I decided to inject the contrast agent gadolinium into the left nodose ganglion in order to see if gadolinium enhanced the left NTS region like manganese. Initially, I tried a 1.0µl low dose injection of gadolinium, which was similar to preclinical studies. However, the dose did not produce enough tissue contrast for this application, so I investigated using a 500mM dose. The Figure 22 below shows results for one of the control rats at 24 hours post-injection. This rat was sacrificed before injection in order to ensure that comparison to the manganese results was as exact as possible.

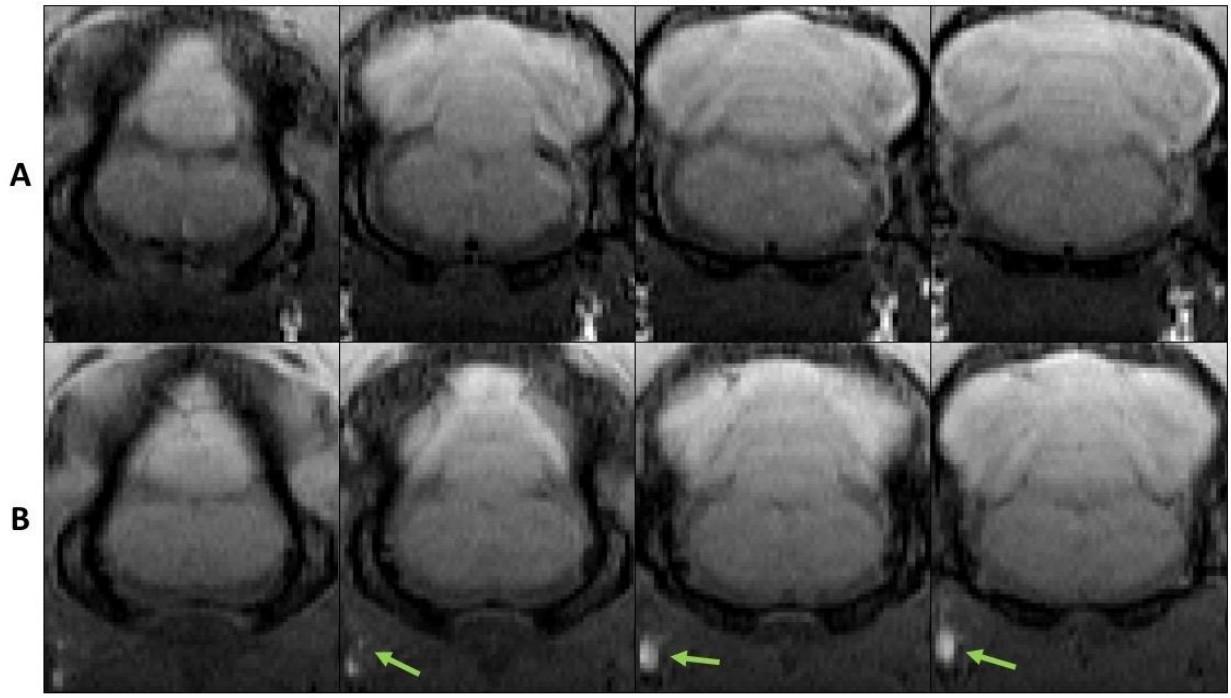

Figure 22. Single subject comparison of baseline and 24 hours post-injection gadolinium accumulation.

(A). This row of brainstem images were the T_1-weighted MR images at baseline. The left most image was the most caudal, and as the images progress towards the right, the location moved more rostral. (B). This row of brainstem images consisted of the T_1-weighted MR images at 24 hours post-injection of 1.0µl of 500mM gadolinium into the left nodose ganglion. The images were manually matched to the baseline images and also progress from caudal to rostral, from left to right. Notice the positive enhancement within the nodose ganglion (green arrow), but nowhere else.

After comparing the Mn^{2+} injected rats to the Gd injected rats, it is clear that the manganese transport from along the vagus nerve to the brain stem was verified. The control rats showed clear enhancement within the injection site, which was supposed to occur, but no enhancement elsewhere. Therefore, the gadolinium was unable to transport along the nerve and did not act like manganese, a calcium analogue.

3.3 Investigation of Second-order Manganese Transport

The previous rats had been sacrificed at 24 hours post-injection, so it was unknown if the manganese enhancement had peaked within the NTS, or if the manganese could transport to further, second-order areas within the brain. Therefore, I designed another experiment in order to optimize the post-injection imaging times. I had hypothesized that after 24 hours post-injection the manganese would accumulate more bilaterally within the NTS region, or that the manganese would transport further to other specific regions within the midbrain.

The figure below shows the results of this experiment. The rat received an injection of 1.0µl of 500mM $MnCl_2$ into the left nodose ganglion and was imaged at post-injection times of 12 hours, 24 hours, and 48 hours. By adding the 12 hours post-injection imaging session, I could observe if enhancement within the left NTS peaked before the 24 hours post-injection time. Furthermore, by adding the 48 hours post-injection time, I could observe if enhancement within the left NTS peaked after the 24 hours post-injection time, and if manganese could travel to second-order brain areas. As can be seen in Figure 24, the 12 hours post-injection time showed a visually stronger enhancement within the left NTS than the 24 hours post-injection time. Additionally, when visually comparing the 24 hours data to the 48 hours data, it was clear that there was less enhancement within the NTS area at 48 hours. Furthermore, there was one rat that showed accumulation of Mn^{2+} in more rostral slices of the brain, but this result was not repeatable. This possible second-order enhancement can be seen in Figure 23. Overall, no other second-order brain areas in the midbrain or forebrain showed a clear, visual enhancement.

I concluded that peak manganese enhancement within the NTS occurred near the 12 hours mark, which demonstrated fast axonal transport, and that after 24 hours, there was not significant transport of manganese from the injection site to the ipsilateral NTS. Therefore, imaging at 48 hours post-injection was not helpful. In order to find areas of possible second-order enhancement, I needed to move onto a more robust group-level analysis.

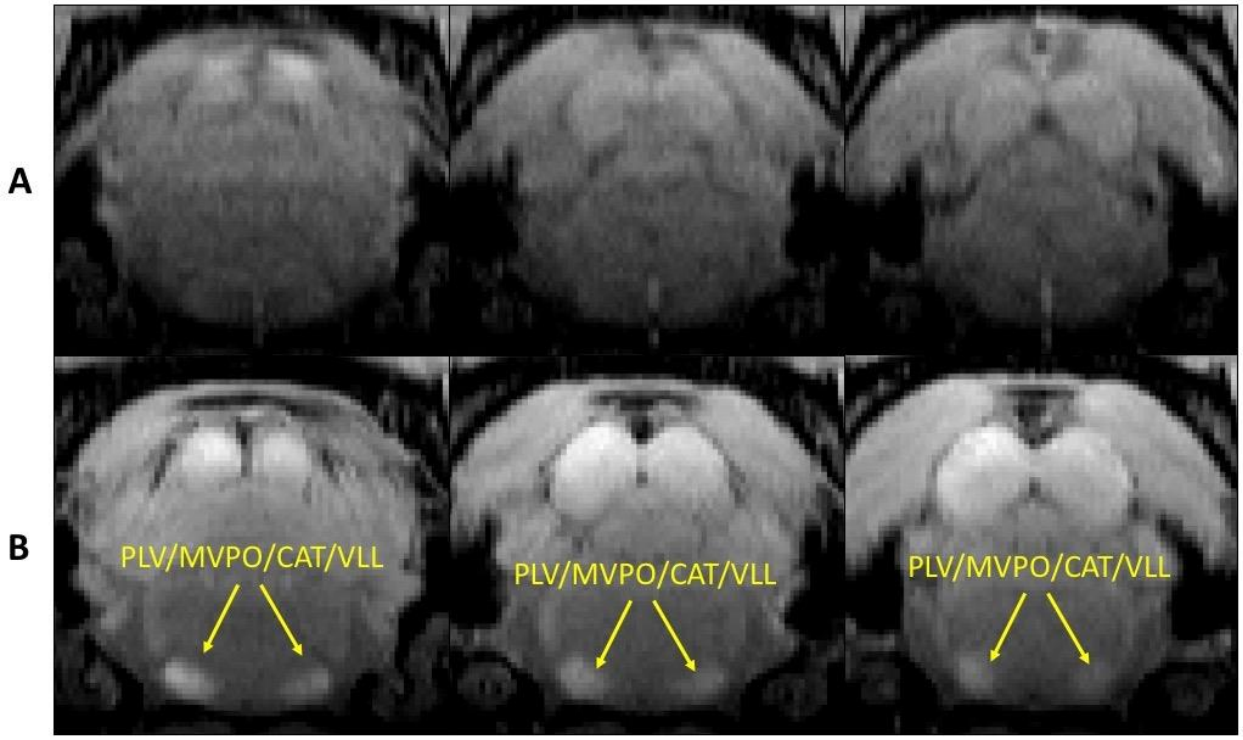

Figure 23. Single subject comparison of possible second-order enhancement.

(A). This row of brainstem images were the T_1-weighted MR images at baseline. The left most image was the most caudal, and as the images progress towards the right, the location moved more rostral. (B). This row of brainstem images consisted of the T_1-weighted MR images at 24 hours post-injection of 1.0µl of 500mM $MnCl_2$ into the left nodose ganglion. Notice the enhancement of the PLV, MVPO, CAT, and VLL brain region. This is approximately located at Interaural 0.24 mm, Bregma -8.76. Abbreviations: PLV=perilemniscal nu, ventral part; MVPO=medioventral periolivary nu; CAT=nu of the central acoustic tract; VLL=ventral nu of lateral lemniscus.

Figure 24. Single subject comparison of baseline, 12 hours post-injection, 24 hours post-injection, and 48 hours post-injection manganese transport.

(A). This row of brainstem images were the T_1-weighted MR images at baseline. The left most image was the most caudal, and as the images progress towards the right, the location moved more rostral. (B). This row of brainstem images consisted of the T_1-weighted MR images at 12 hours post-injection of 1.0µl of 500mM $MnCl_2$ into the left nodose ganglion. (C). This row of brainstem images consisted of the T_1-weighted MR images at 24 hours post-injection of 1.0µl of 500mM $MnCl_2$ into the left nodose ganglion. (D). This row of brainstem images consisted of the T_1-weighted MR images at 48 hours post-injection of 1.0µl of 500mM $MnCl_2$ into the left nodose ganglion. Note: all of these images were manually matched to the baseline images and progress from caudal to rostral, from left to right across the row. Notice the positive enhancement within the left nodose ganglion (green arrow), along the fiber tract (red arrow), large enhancement in the left NTS (yellow arrow), and small enhancement in the right NTS (orange arrow).

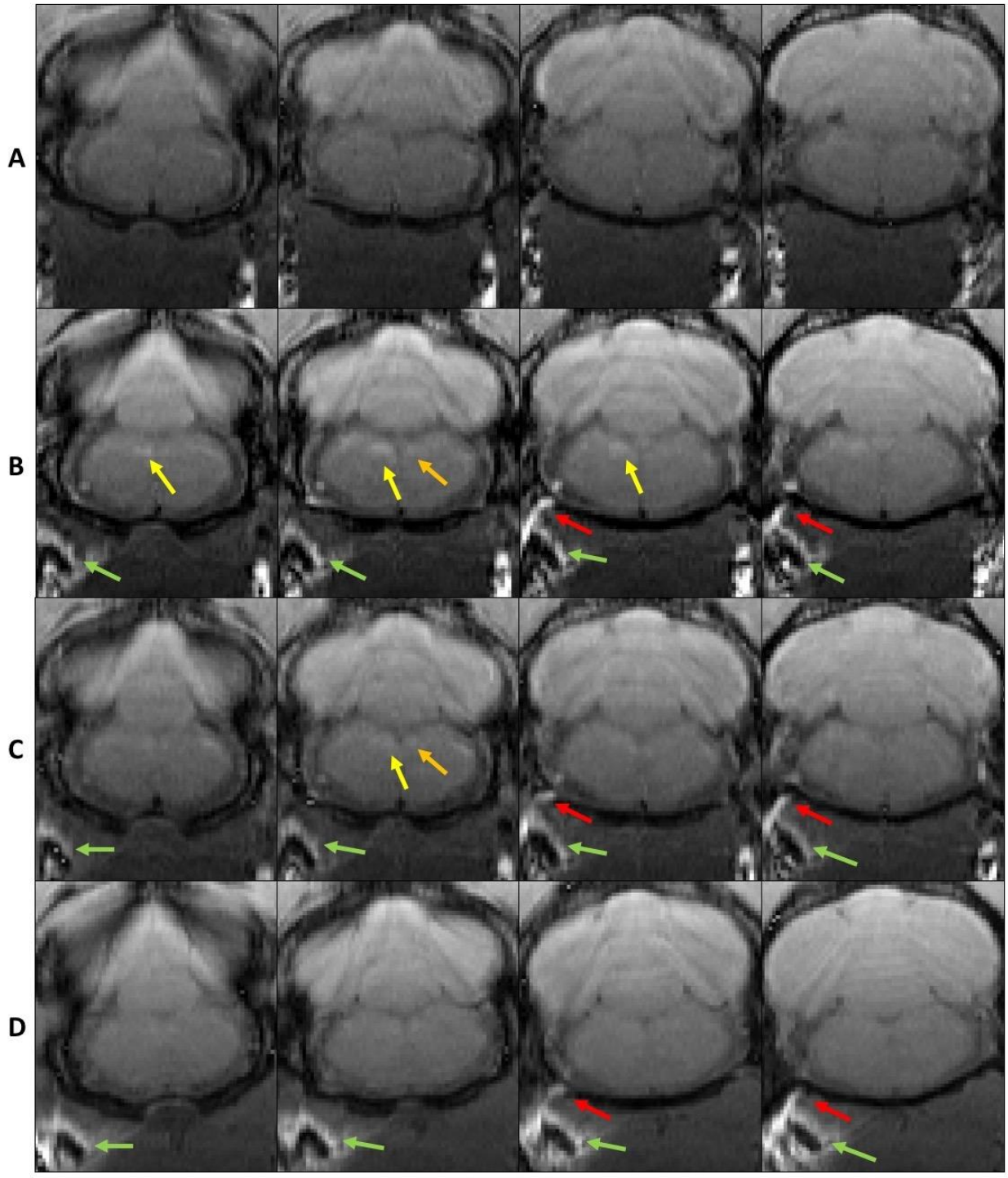
A
B
C
D

3.4 Comparison Between Experimental Groups

When I compared pre-injection images of the rat brain with the corresponding post-injection images, it was apparent that manganese was transported from the side-specific injection site to the ipsilateral NTS. The first group showed an increase in the normalized signal intensity in the left NTS at 12 hours post-injection (42.64%, $p<0.02$). The second group also showed an increase in the normalized signal intensity in the left NTS at 12 hours post-injection, but at a lesser magnitude (23.82%, $p<0.02$). The third group resulted in an observed enhancement in the right NTS at 12 hours post-injection at a similar magnitude to the second group's respective enhancement (24.72%, $p<0.02$). Additionally, at a group-level, I observed smaller enhancement within the contralateral NTS to the injection site, proving that there was a cross-synaptic transport of Mn^{2+}.

3.4.1 Group 1 – Single Subject Sample

The following is a single subject example from experimental group 1. This is the group that was injected into the left nodose ganglion and received VNS for a period of four hours. The Figure 25 shows the T_1-weighted MR images at baseline, 12 hours post-injection, and 24 hours post-injection.

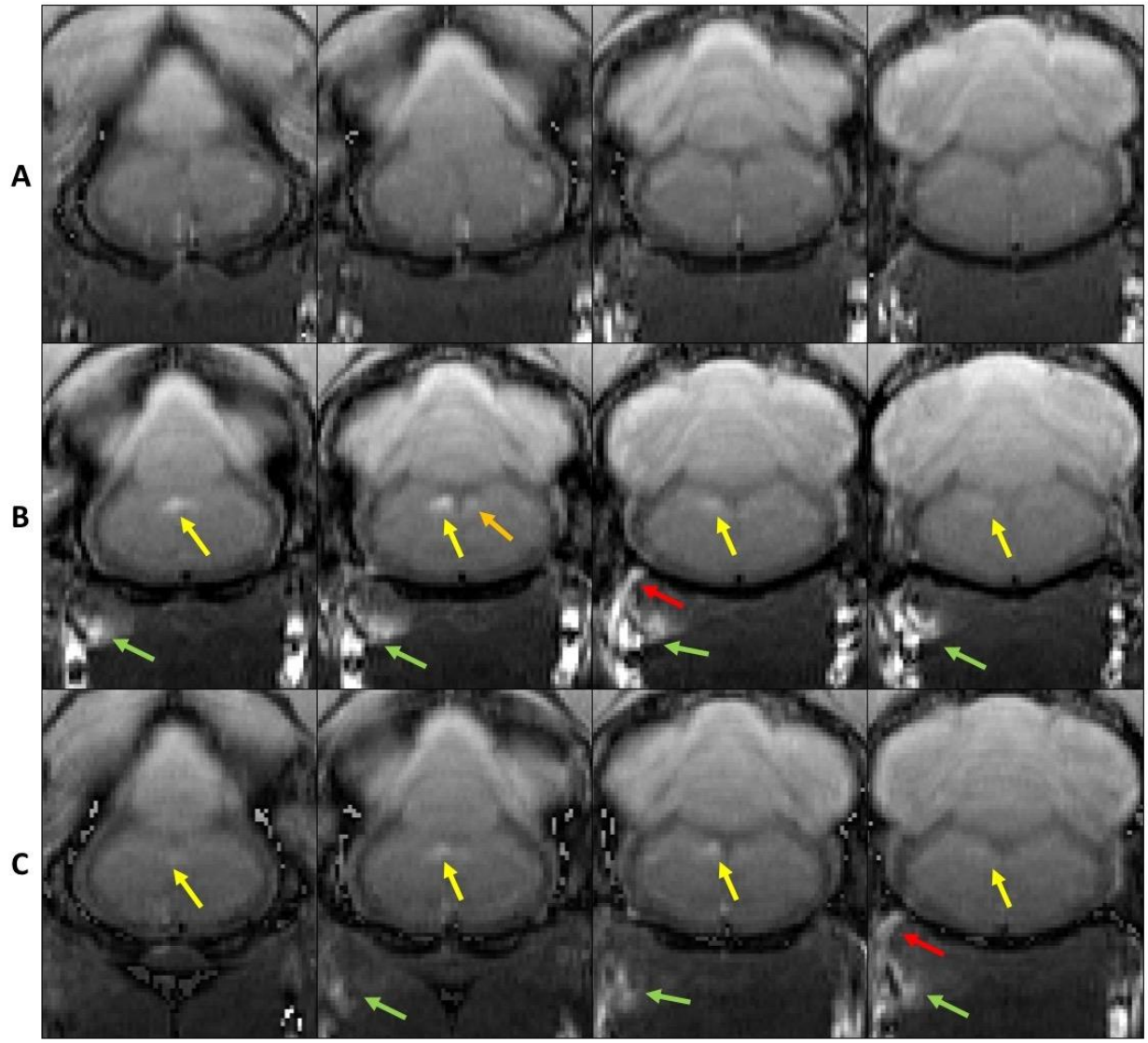

Figure 25. Single subject comparison of baseline, 12 hours post-injection, and 24 hours post-injection manganese transport for group 1.

(A). This row of brainstem images were the T_1-weighted MR images at baseline. The left most image was the most caudal, and as the images progress towards the right, the location moved more rostral. (B). This row of brainstem images consisted of the T_1-weighted MR images at 12 hours post-injection of 1.0µl of 500mM $MnCl_2$ into the left nodose ganglion. (C). This row of brainstem images consisted of the T_1-weighted MR images at 24 hours post-injection of 1.0µl of 500mM $MnCl_2$ into the left nodose ganglion. Note: all of these images were manually matched to the baseline images and progress from caudal to rostral, from left to right across the row. Notice the positive enhancement within the left nodose ganglion (green arrow), along the fiber tract (red arrow), large enhancement in the left NTS (yellow arrow), and small enhancement in the right NTS (orange arrow).

3.4.2 Group 2 – Single Subject Sample

The following is a single subject example from experimental group 2. This is the group that was injected into the left nodose ganglion, but did not receive VNS. The Figure 26 shows the T_1-weighted MR images at baseline, 12 hours post-injection, and 24 hours post-injection. It is difficult to visually see if there is a difference in accumulation between this single subject and the single subject from experimental group 1. Therefore, an analysis was used to quantify differences on a group-level.

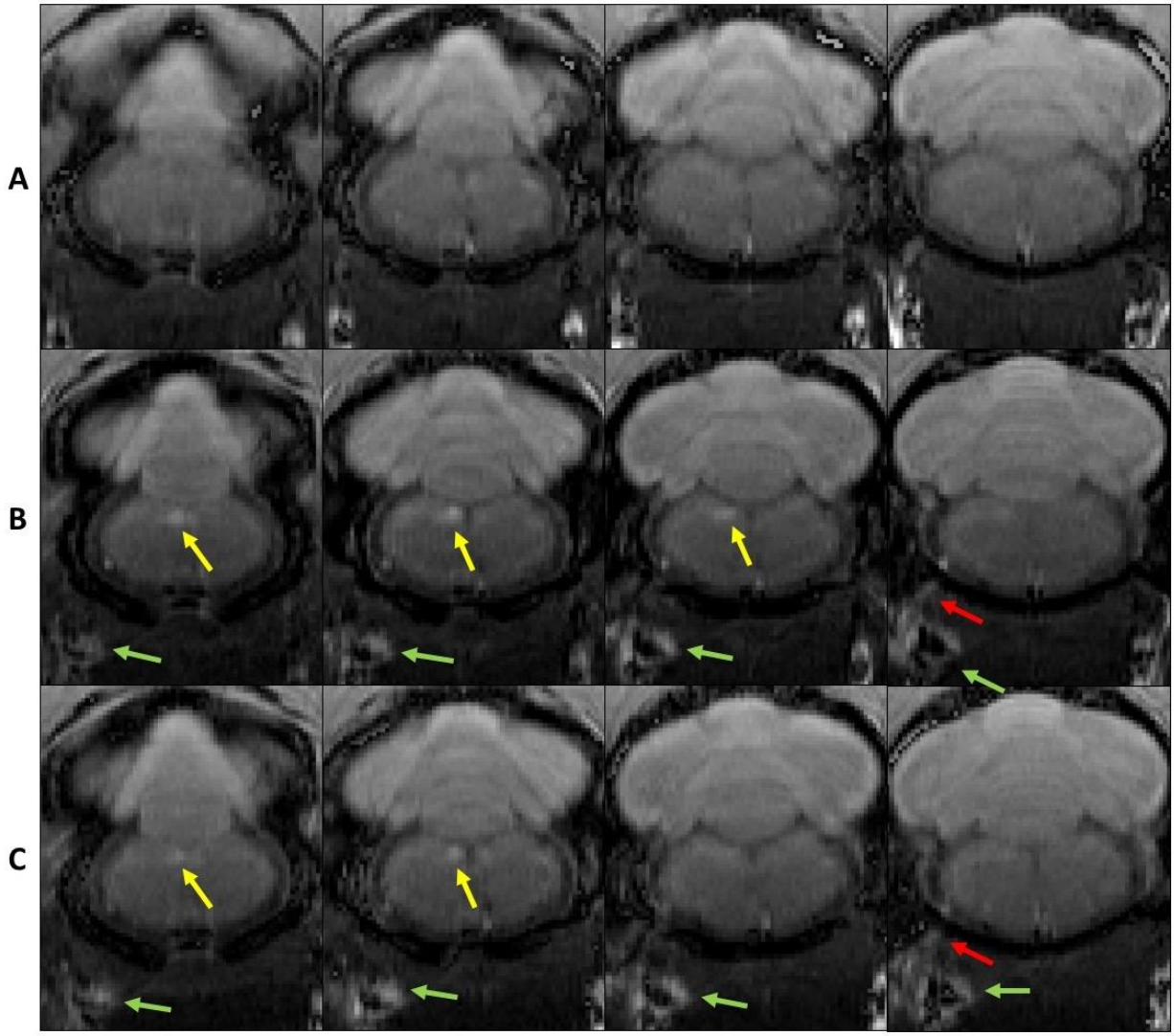

Figure 26. Single subject comparison of baseline, 12 hours post-injection, and 24 hours post-injection manganese transport for group 2.

(A). This row of brainstem images were the T_1-weighted MR images at baseline. The left most image was the most caudal, and as the images progress towards the right, the location moved more rostral. (B). This row of brainstem images consisted of the T_1-weighted MR images at 12 hours post-injection of 1.0µl of 500mM $MnCl_2$ into the left nodose ganglion. (C). This row of brainstem images consisted of the T_1-weighted MR images at 24 hours post-injection of 1.0µl of 500mM $MnCl_2$ into the left nodose ganglion. Note: all of these images were manually matched to the baseline images and progress from caudal to rostral, from left to right across the row. Notice the positive enhancement within the left nodose ganglion (green arrow), along the fiber tract (red arrow), large enhancement in the left NTS (yellow arrow), and small enhancement in the right NTS (orange arrow).

3.4.3 Group 3 – Single Subject Sample

The following is a single subject example from experimental group 3. This is the group that was injected into the right nodose ganglion and did not undergo VNS. The Figure 27 shows the T_1-weighted MR images at baseline, 12 hours post-injection, and 24 hours post-injection.

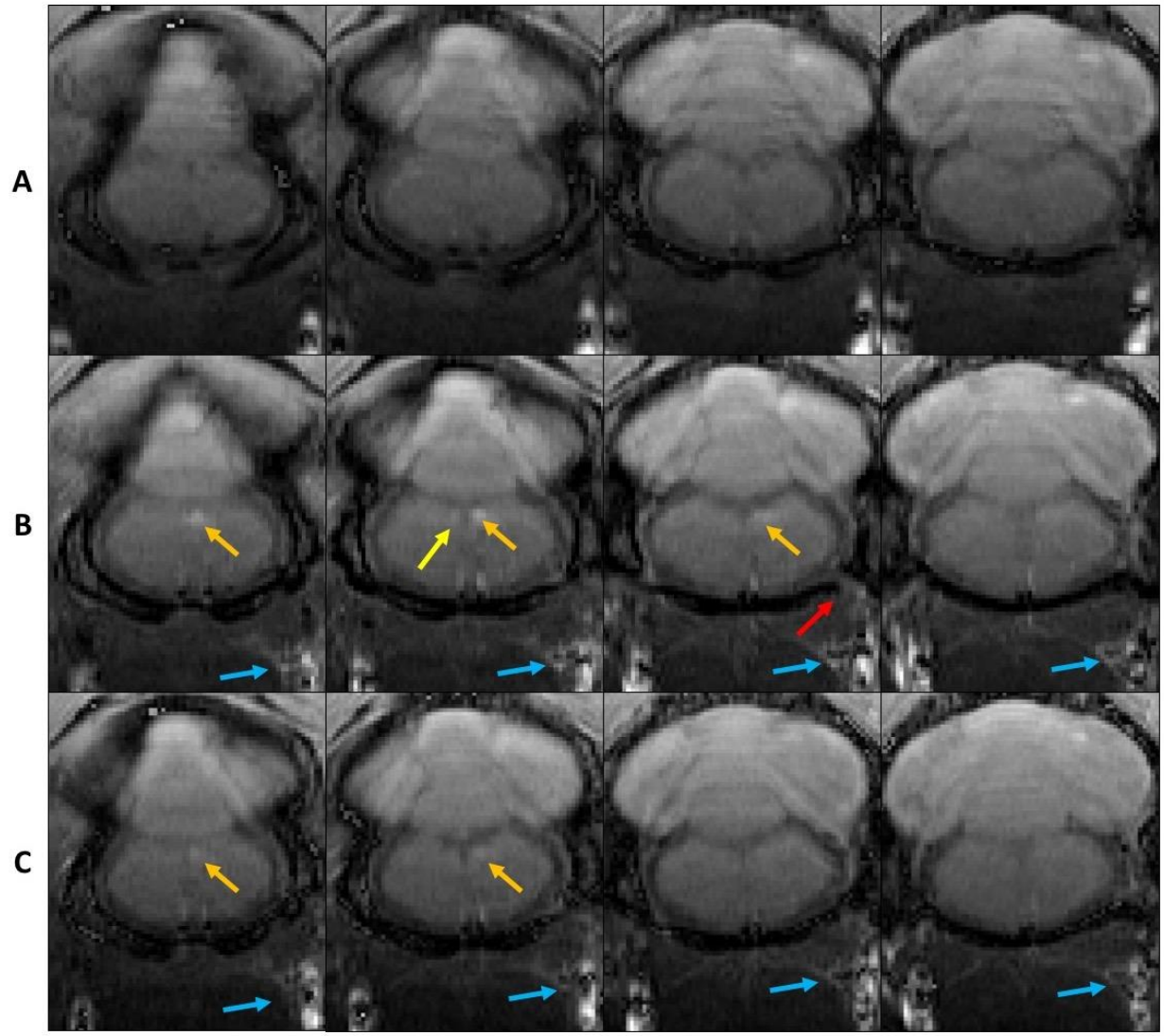

Figure 27. Single subject comparison of baseline, 12 hours post-injection, and 24 hours post-injection manganese transport for group 3.

(A). This row of brainstem images were the T_1-weighted MR images at baseline. The left most image was the most caudal, and as the images progress towards the right, the location moved more rostral. (B). This row of brainstem images consisted of the T_1-weighted MR images at 12 hours post-injection of 1.0µl of 500mM $MnCl_2$ into the right nodose ganglion. (C). This row of brainstem images consisted of the T_1-weighted MR images at 24 hours post-injection of 1.0µl of 500mM $MnCl_2$ into the right nodose ganglion. Note: all of these images were manually matched to the baseline images and progress from caudal to rostral, from left to right across the row. Notice the positive enhancement within the right nodose ganglion (blue arrow), along the fiber tract (red arrow), large enhancement in the right NTS (orange arrow), and minimal enhancement in the left NTS (yellow arrow).

3.4.4 Injection Site Specific Enhancement Patterns in the NTS

The following Figure 28 and 29 show the results comparing the brainstem enhancement patterns between group 2 and group 3 at the peak enhancement time, 12 hours post-injection. The top row showed an enhancement within its ipsilateral left NTS (23.82%, $p<0.02$). The bottom row showed an enhancement within its ipsilateral right NTS (24.72%, $p<0.02$). Notice the strongest accumulation occurs on the same side of injection.

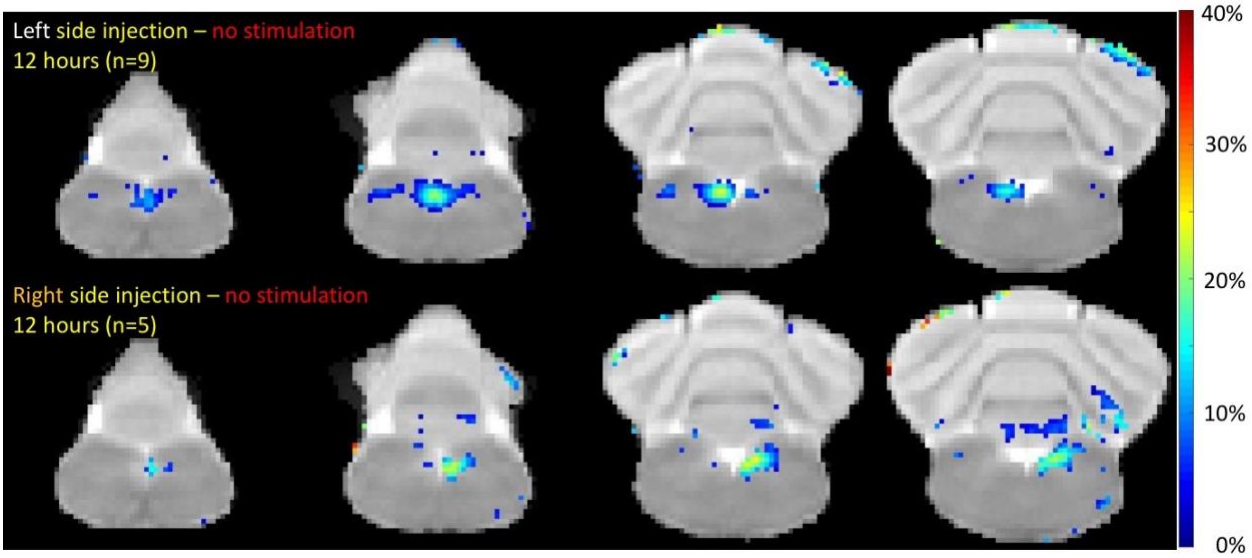

Figure 28. Group-level map demonstrating the injection site specific enhancement patterns in the NTS.

The top row consisted of a group-level enhancement map in the NTS for group 2 at 12 hours post-injection. The bottom row consisted of a group-level enhancement map in the NTS for group 3 at 12 hours post-injection. All enhanced voxels are significant at a $p<0.02$.

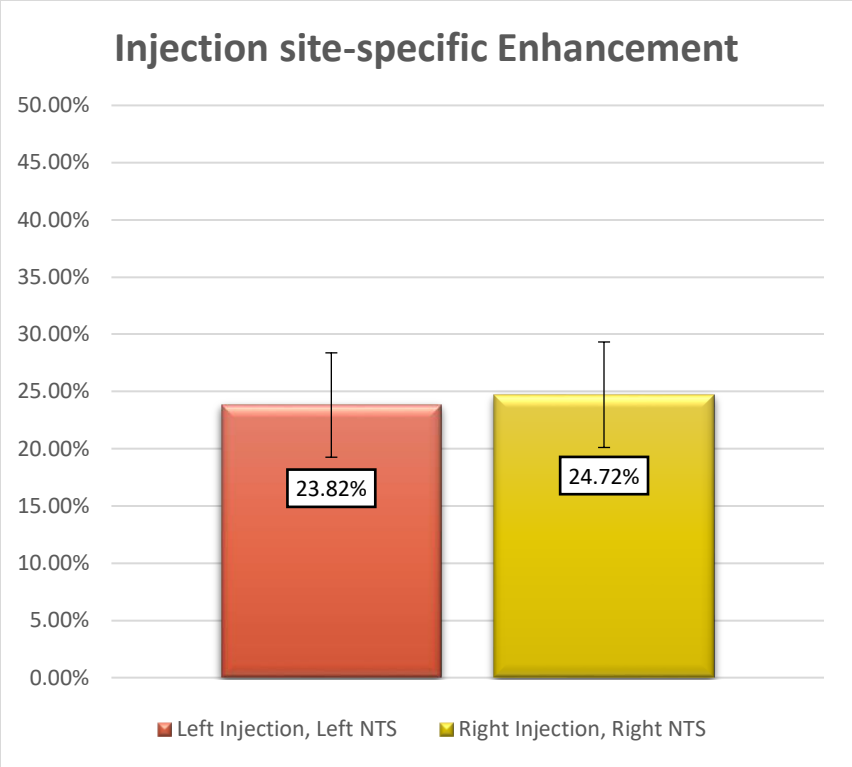

Figure 29. Graph showing the quantified enhancement patterns in the ipsilateral NTS between groups 2 and 3 at 12 hours post-injection.

3.4.5 Stimulation Increases Enhancement in the NTS

The following Figure 30 and 31 show the results comparing the brainstem enhancement patterns between group 2 and group 1 at the peak enhancement time, 12 hours post-injection. The top row showed an enhancement within its ipsilateral left NTS (23.82%, $p<0.02$). The bottom row showed an enhancement within its ipsilateral left NTS (42.64%, $p<0.02$). Therefore, group-level analysis confirmed that VNS promoted the transport of manganese.

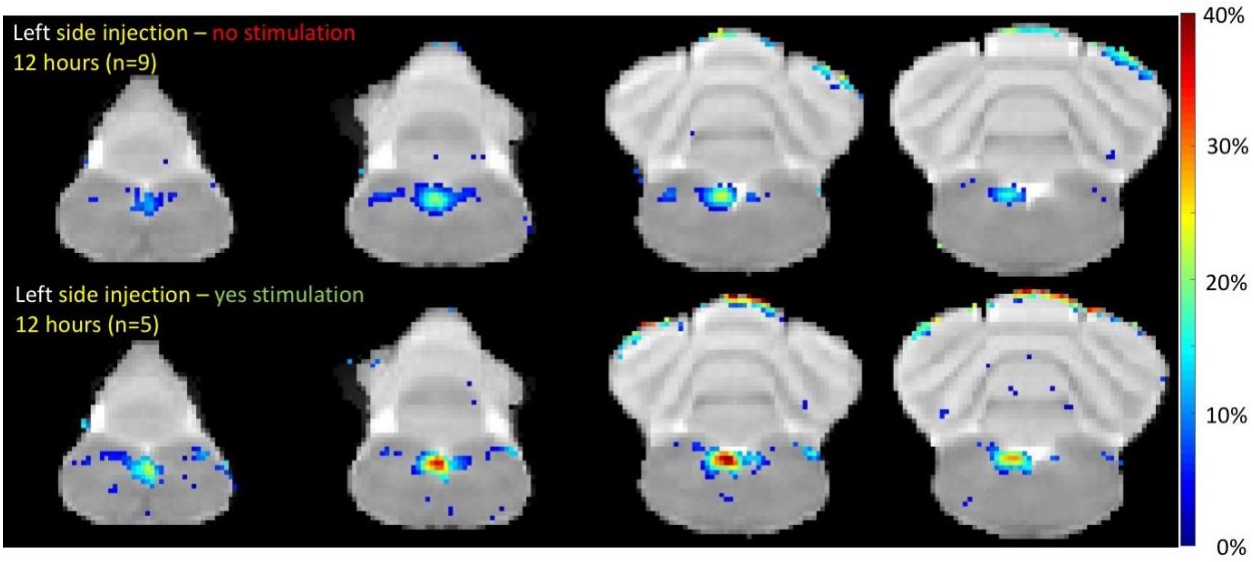

Figure 30. Group-level map demonstrating the enhancement changes from VNS.

The top row consisted of a group-level enhancement map in the NTS for group 2 at 12 hours post-injection. The bottom row consisted of a group-level enhancement map in the NTS for group 1 at 12 hours post-injection. All enhanced voxels are significant at a $p<0.02$.

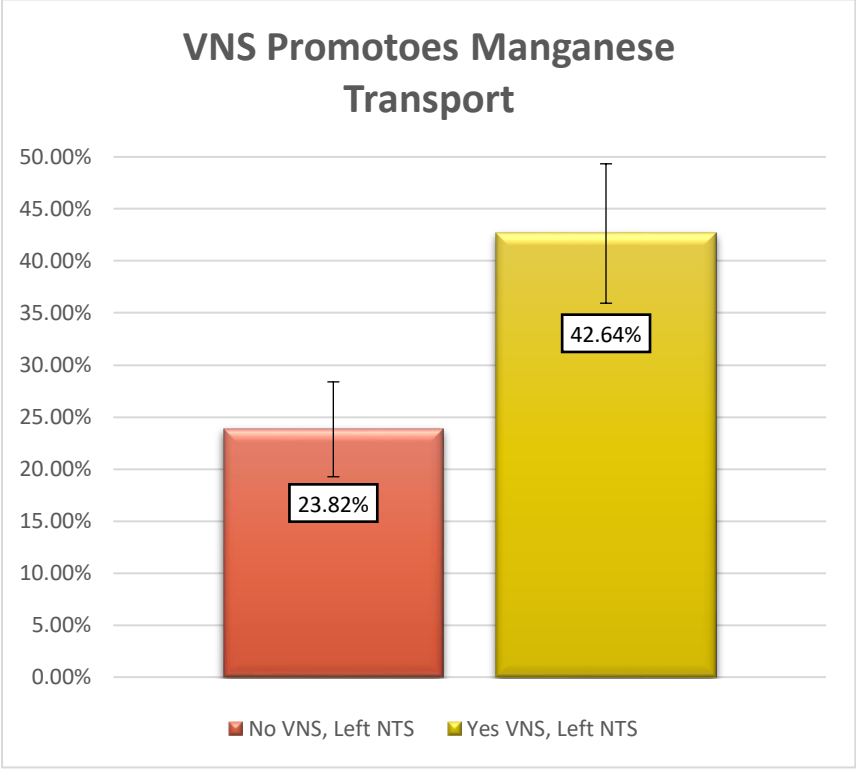

Figure 31. Graph showing the quantified enhancement patterns in the ipsilateral NTS between groups 2 and 1 at 12 hours post-injection.

3.4.6 Enhancement in the NTS Peaks at 12 Hours Post-injection

The Figure 32 and 33 show the results comparing the brainstem enhancement patterns for group 2 at different imaging times of 12 hours post-injection and 24 hours post-injection. The top row showed an ipsilateral enhancement within the left NTS (23.82%, $p<0.02$). The bottom row showed a similar level of ipsilateral enhancement within the left NTS (21.91%, $p<0.02$). Notice the accumulation decreased after the 12 hours post-injection time.

The Figure 34 and 35 show the results comparing the brainstem enhancement patterns for group 1 at different imaging times of 12 hours post-injection and 24 hours post-injection. The top row showed an ipsilateral enhancement within its left NTS (42.64%, $p<0.02$). The bottom row showed a similar level of ipsilateral enhancement within its left NTS (39.98%, $p<0.02$). Again, notice the accumulation decreased the 12 hours post-injection time.

These results showed that Mn^{2+} transport was fast, axonal transport.

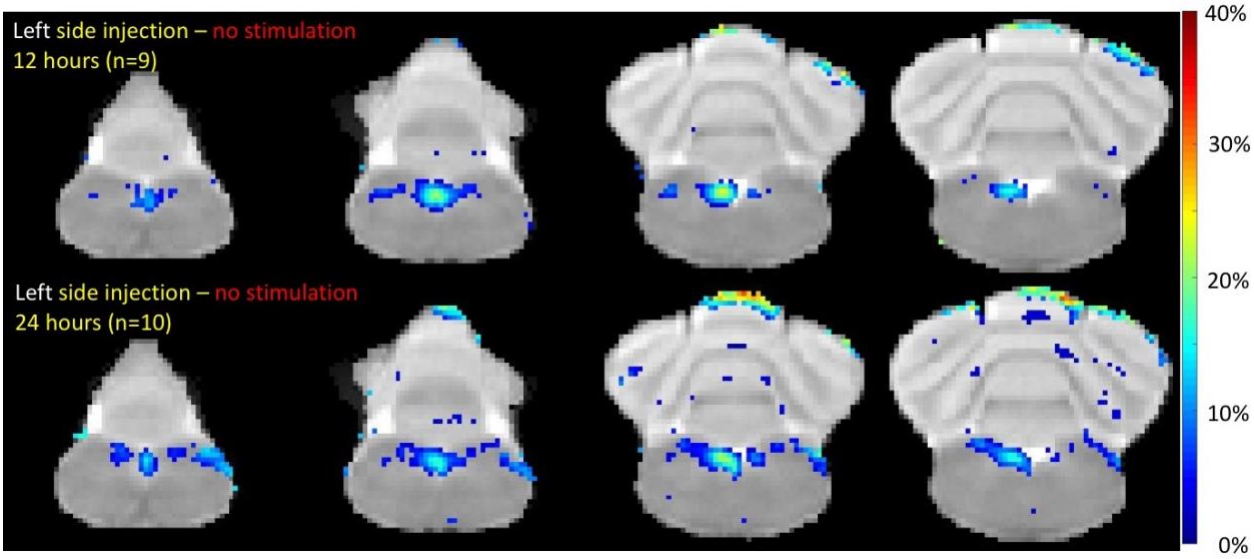

Figure 32. Group-level map demonstrating the enhancement changes between 12 hours and 24 hours for experimental group 2.

The top row consisted of a group-level enhancement map in the NTS for group 2 at 12 hours post-injection. The bottom row consisted of a group-level enhancement map in the NTS for group 2 at 24 hours post-injection. All enhanced voxels are significant at a $p<0.02$.

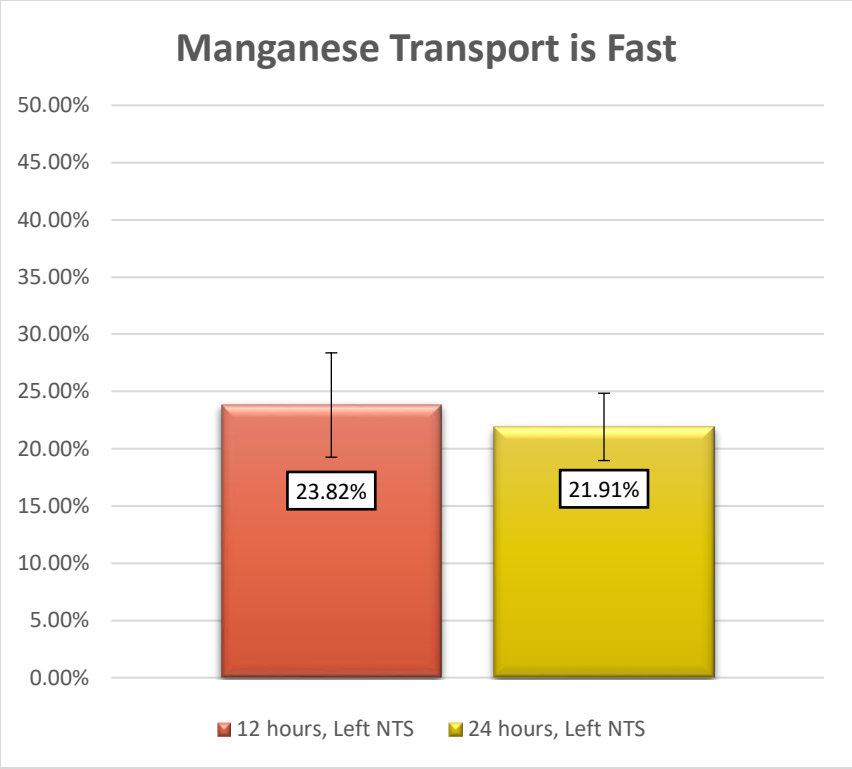

Figure 33. Graph showing the quantified enhancement patterns in the ipsilateral NTS between the 12 hours and 24 hours post-injection times for group 2.

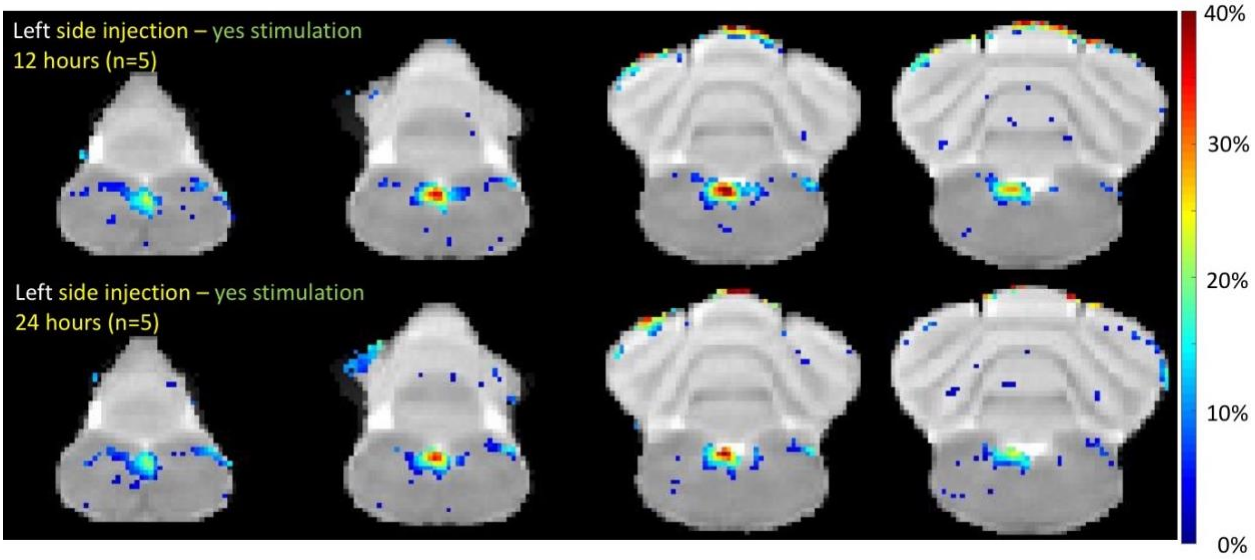

Figure 34. Group-level map demonstrating the enhancement changes between 12 hours and 24 hours for experimental group 1.

The top row consisted of a group-level enhancement map in the NTS for group 1 at 12 hours post-injection. The bottom row consisted of a group-level enhancement map in the NTS for group 1 at 24 hours post-injection. All enhanced voxels are significant at a $p<0.02$.

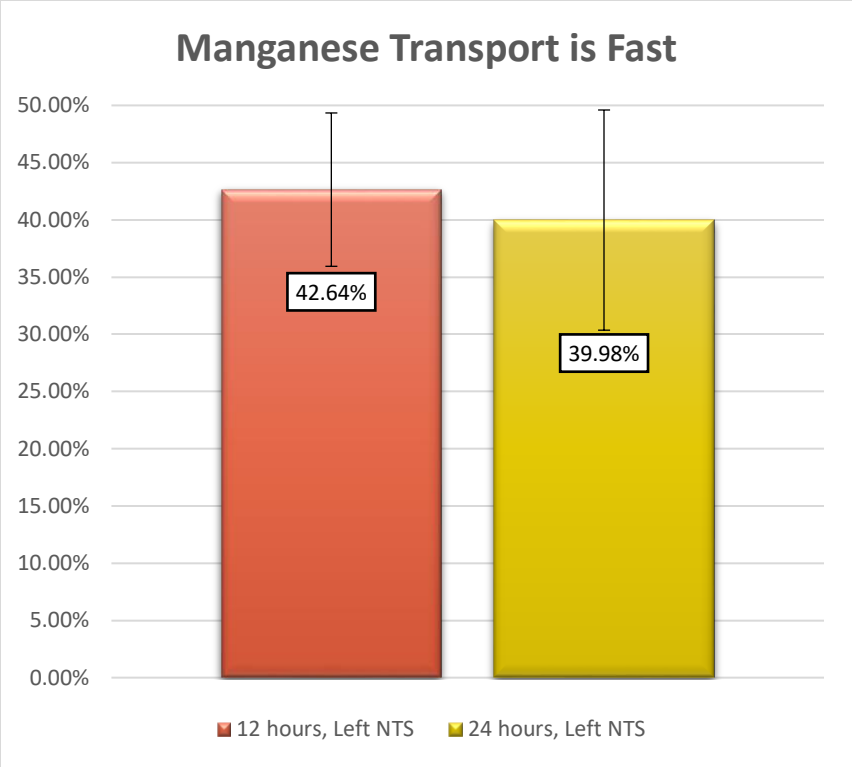

Figure 35. Graph showing the quantified enhancement patterns in the ipsilateral NTS between the 12 hours and 24 hours post-injection times for group 1.

3.5 Histological Validation

A method for validating the manganese accumulation within the brainstem was investigated. The method that was investigated was the Timms Sulphide Silver Stain. This stain is used to visualize heavy metals within the brain and other tissues. As can be seen in the Figure 36, there are a large number of stained cells for the control rats, the least amount of stained cells for the rats sacrificed at 12 hours post-injection, and a medium amount of stained cells for the rats sacrificed at 24 hours post-injection.

Figure 36. Coronal brain sections after completion of the Timms Sulphide Silver staining.

This montage shows the of heavy metals within the NTS region. Each panel is a slice from a different rat. Results from a total of six rats are shown (A). Stained sections from control rats that were not injected. (B). Stained sections from rats that were injected with 1.0µl of 500mM $MnCl_2$ into the left nodose ganglion. Rats were perfused at 12 hours post-injection. (C). Stained sections from rats that were injected with 1.0µl of 500mM $MnCl_2$ into the left nodose ganglion. Rats were perfused at 24 hours post-injection.

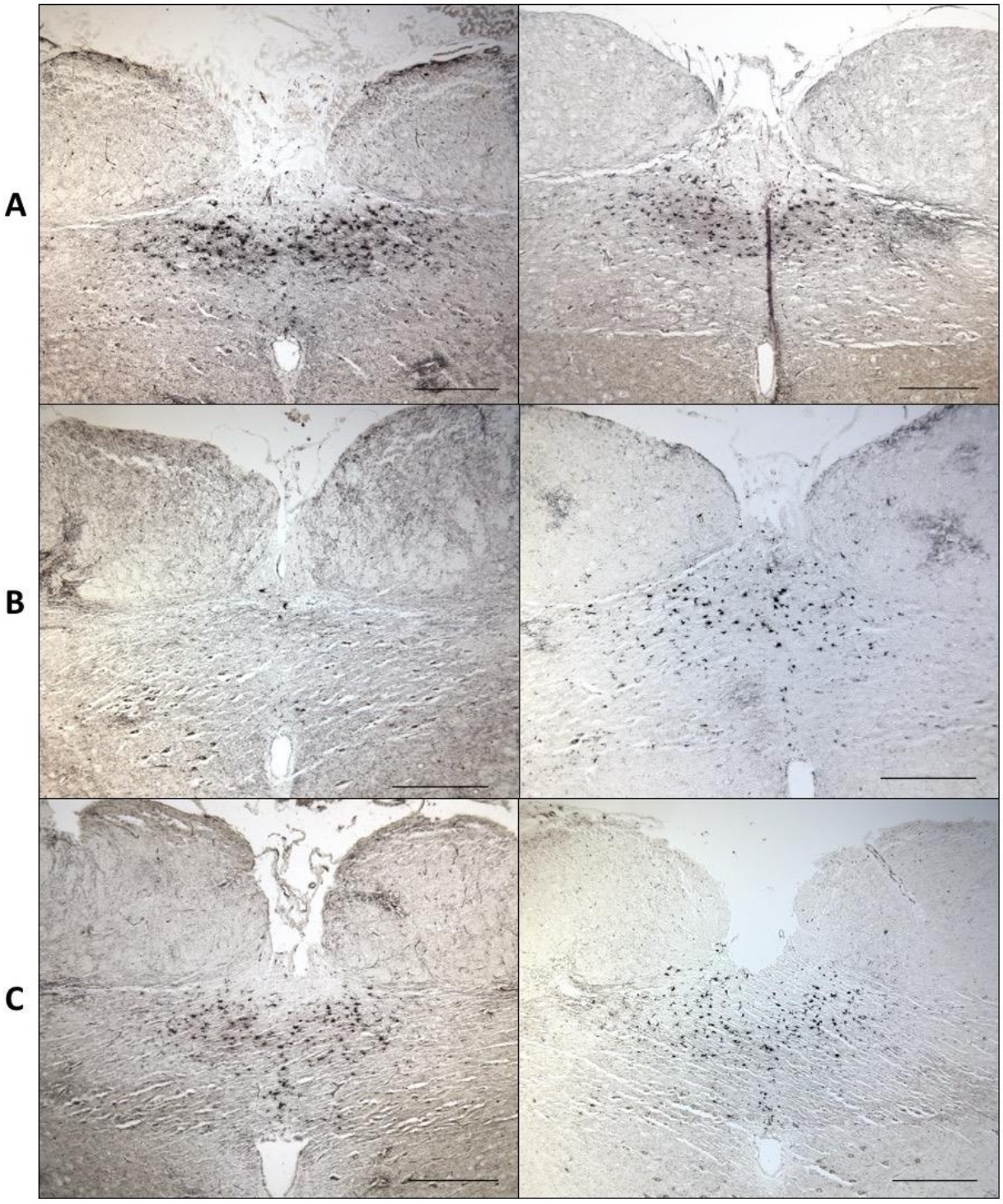
A
B
C

3.6 Downstream Projection of the Sympathetic Pathway

During these experiments, the rats showed a dot of enhancement running caudally from the brain stem. This dot of enhancement is shown by the red arrow in the T_1-weighted MR images from a sample rat at 12 hours post-injection. This is the first time that the spinal nerve tract has been presented with MEMRI. It is important to note that the 3D view of the brain makes it look like the afferent projection of the vagus nerve is connected with the spinal tract. However, this is not the case.

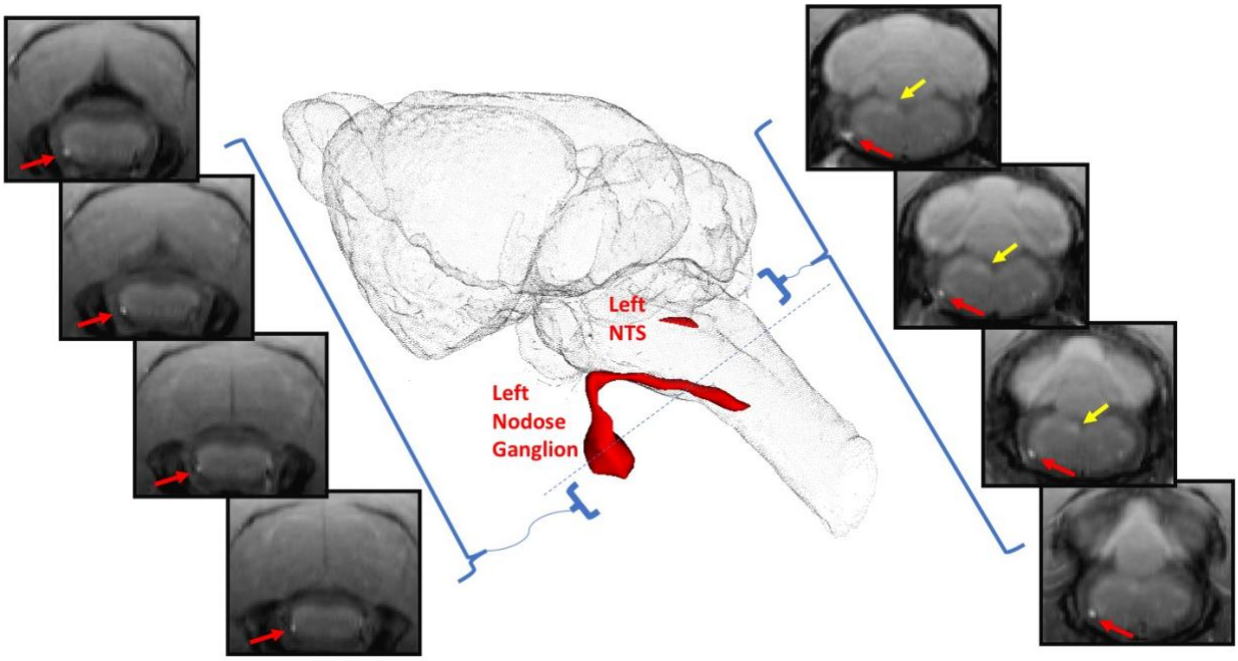

Figure 37. Retrograde spinal pathway enhancement.

The T_1-weighted MR images of a rat subject at 12 hours post-injection are shown along with the 3D constructed brain. In the MR images, the red arrow is pointing to a bright dot, which is the enhanced spinal nerve pathway. The yellow arrow is pointing to enhancement within the ipsilateral NTS. In the 3D constructed brain, the enhancement of the injection site, vagal fiber tract running up to the brainstem, the downward projection of the spinal nerve tract, and the left NTS are shown in red.

4. TAKEAWAYS AND CONCLUDING REMARKS

4.1 Overall Takeaways

After seeing all of the experimental design and results, there are multiple points to understand from this work. I was able to optimize the hardware design used for the experimental setup, master the microinjection surgical technique, optimize post-injection imaging times, observe group-level specific enhancement patterns within the brainstem, explore histological validation, and show enhancement of the spinal nerve tract.

4.1.1 Takeaways: Experimental Design

I was able to optimize image quality for regions of interest within the brainstem. The brainstem is subject to more motion that other parts of the brain, like the cortex, because it is closer to the neck, which moves when the animal breathes. By incorporating design requirements and constraints into a carefully planned, and iterative design approach, I was able to design a modified restraint system that minimized motion better than commercially sold holders. This hardware design incorporated 3D printed parts that were able to account for rats of a large range of sizes. Additionally, I manufactured a bite bar and ears bars out of PEEK material, which had an extremely high tensile strength to negate any bending. As can be seen in the MR images shown throughout this thesis, there were no motion artifacts, even at the most caudal portions of the brainstem and along the spine.

One of the more challenging, hands-on, aspects of this study was having to learn the surgery procedure and micro-injection. This required lots of practice, steady hands, and tons of learning in order to understand when the injections were successful. The ability to have mastered the micro-injection procedure was particularly great for minimizing adverse effects to the rats. Additionally, I was able to confirm my micro-injection approach and results with an experienced research technician who had completed thousands of nodose ganglion injections. The imaging timeline was also optimized, which allowed me to limit the amount of MRI sessions and determine when the manganese enhancement peaked in the brainstem.

4.1.2 Takeaways: Enhancement Patterns

I originally hypothesized that the transport of Mn^{2+} would lead to a higher level of enhancement as time progressed after injection. Additionally, I hypothesized that after a group-level analysis, it would be possible to pinpoint specific areas outside of the brainstem that were sites of Mn^{2+} accumulation. However, from the group-level analysis, it is clear that the accumulation of Mn^{2+} within the NTS region did not increase after 12 hours post-injection. Additionally, there were no specific regions of enhancement in other areas of the brain. There are a few possibilities as to why this might have occurred.

First, the Mn^{2+} that had accumulated within the NTS at 12 hours post-injection could have progressively diffused out of the NTS region to nearby brain tissue. This would have resulted in a less localized accumulation of Mn^{2+} and more of a widespread enhancement within that region. Therefore, there might not have been enough Mn^{2+} for continued observable transport along the pathway because it was diffusing out.

Second, the Mn^{2+} that had accumulated within the ipsilateral NTS at 12 hours post-injection might not have been taken up within the contralateral NTS very efficiently. Thus, only a small amount of manganese was able to transport across the synapse. This would explain the reason why there was not a large amount of accumulation within the contralateral NTS. This would also explain why there were no other specific areas of enhancement within the midbrain. There simply isn't enough Mn^{2+} that is transporting from the ipsilateral NTS across the synapse to the contralateral NTS.

Third, the Mn^{2+} concentration is either too high, or too low. The Mn^{2+} concentration was assessed based off contrast to the ipsilateral NTS and by adverse behavioral and visual effects of the rats. However, it might be important to explore a multitude of different concentrations. For example, if the concentration of Mn^{2+} was too high, then the cells within the nodose ganglion or in the nerve tract might be going necrotic. If these cells are dying, then it would be impossible for the Mn^{2+} to continually transport. Additionally, if the concentration was too low, then the tissue concentration might be too low after the Mn^{2+} has transported past the ipsilateral NTS. This would make it impossible to observe further transport.

4.1.3 Takeaways: Histological Validation

I explored using the Timms Sulphide Silver stain to observe cells within the brainstem and other areas of the brain that accumulated Mn^{2+}. This stain uses the histochemical transformation of metals to metal sulphides to visualize metals at the cellular level. I had hypothesized that the group-level MRI data that corresponded to the largest enhancement within the ipsilateral NTS region would also correspond to the sections with the greatest number of stained cells. This was not the case. In fact, the opposite relationship occurred. The control rats showed a high level of stained cells within the bilateral NTS, the 12 hours post-injection rats had the smallest number of stained cells, and the 24 hours post-injection rats showed a medium number of stained cells. This means that the number of cells being visualized by the stain was suppressed, and then increased with post-injection time.

A possible explanation for how this occurred has to do with the specificity and sensitivity of the Timms stain to Mn^{2+}. The Timms Silver Sulphide stain can visualize a variety of metals within the brain and is not specific to any one metal. Some of these metals are Zn, Cu, Fe, Co, and Ni. I believe that the stain was more sensitive to other metals within the NTS region of the brain and was primarily detecting trace metals that were not Mn^{2+}. Therefore, when the Mn^{2+} accumulation peaked at 12 hours post-injection, the other trace metals within the NTS region were suppressed. Furthermore, the control sections showed a high visualization of metals because there was no Mn^{2+} presence to take the place of the other metals.

4.1.4 Takeaways: Tracing the Spinal Nerve

Tracing the downstream projection of the sympathetic pathway from the brainstem was possible because of the reduced motion during this study. The enhanced spinal nerve may be proof of *in vivo* anterograde and retrograde transportation of the manganese. The T_1-weighted MR images of the sample rat subject show that Mn^{2+} anterogradely transported from the left nodose ganglion, along the vagus fiber tract, to the NTS region, up taken by the spinal tract, and then retrogradely transported along the spinal nerve caudally. The enhancement shown is most likely not a vagus nerve branch because of how far caudal the enhancement can be traced. This is the first time that MEMRI enhancement of the spinal nerve is being shown in the rodent model.

4.2 Future Work

Future work for this study would continue to focus on exploring secondary sites of enhancement after transport to the NTS region. For this to occur, a specific set of experiments would need to be planned out to first fully optimize the Mn^{2+} injection concentration. This could be done by injecting high levels of concentrations (e.g. 125mM, 250mM, 500mM, 750mM, 1M) into different rats, imaging the rats over 2-3 days, and also implementing a behavioral test to determine if the rats are experiencing adverse effects. The behavioral test could be recording maze navigation times to food targets and then comparing to see if the times significantly increased after injections.

Another set of tests that would help optimize the injection concentration could relate to implementing histology and assays. It would also be interesting to investigate the status of the cells within the site of injection, the vagus nerve, and within the brain stem. This could be done by completing a thionin staining, which would reveal areas of complete cell loss. Additionally, one could also assay the enhanced brain regions in order to determine the concentration of Mn^{2+} in the tissue extracts, which could help compare to the neurotoxic concentrations.

Assuming that the manganese concentration can be fully optimized for this application, it would also be interesting to implement two more sets of experiments. One set of experiments could involve investigating different clinically used VNS parameters. For example, it would be interesting to see if VNS for epilepsy resulted in a different enhancement pattern than VNS for depression. The other experiment would be to figure out a way to chronically implant a slow release mechanism into the nodose ganglion. This would allow for very large doses of Mn^{2+} to be given to the animal, but the slow release would ideally result in farther transport and minimized adverse effects.

4.3 Conclusion

In conclusion, I have shown that the use of MEMRI to quantify the Mn^{2+} transport along peripheral nerves to the brainstem is feasible, specific, neuronal, and activity-dependent. I developed a robust, non-invasive, contrast-enhanced experimental MRI approach to trace neuronal connections in-vivo over time. The potential of this method can lead to understanding how different therapeutic VNS parameters map and activate specific neuronal pathways.

REFERENCES

[1] R. H. Howland, "Vagus Nerve Stimulation," *Curr Behav Neurosci Rep*, pp. 64–73, 2014.

[2] R. L. Johnson and C. G. Wilson, "A review of vagus nerve stimulation as a therapeutic intervention," *J. Inflamm. Res.*, vol. 11, pp. 203–213, 2018.

[3] S. Currie, N. Hoggard, I. J. Craven, M. Hadjivassiliou, and I. D. Wilkinson, "Understanding MRI: Basic MR physics for physicians," *Postgrad. Med. J.*, vol. 89, no. 1050, pp. 209–223, 2013.

[4] "T1 relaxation - Questions and Answers in MRI." [Online]. Available: http://mriquestions.com/what-is-t1.html. [Accessed: 04-Nov-2018].

[5] "T2 (spin-spin) relaxation - Questions and Answers in MRI." [Online]. Available: http://mriquestions.com/what-is-t2.html. [Accessed: 04-Nov-2018].

[6] "MRI Basics." [Online]. Available: http://casemed.case.edu/clerkships/neurology/web neurorad/mri basics.htm. [Accessed: 05-Nov-2018].

[7] R. G. Pautler, A. C. Silva, and A. P. Koretsky, "In vivo neuronal tract tracing using manganese-enhanced magnetic resonance imaging," *Magn. Reson. Med.*, vol. 40, no. 5, pp. 740–748, 1998.

[8] N. Rajakumar, K. Elisevich, and B. A. Flumerfelt, "Biotinylated dextran: a versatile anterograde and retrograde neuronal tracer," *Brain Res.*, vol. 607, no. 1–2, pp. 47–53, 1993.

[9] K. Kristensson and Y. Olsson, "Retrograde axonal transport of protein.," *Brain Res.*, vol. 29, no. 2, pp. 363–5, 1971.

[10] Y. Tillet, M. Batailler, and J. Thibault, "Neuronal Projections To the Medial Preoptic Area of the Sheep, With Special Reference To Monoaminergic Afferents - Immunohistochemical and Retrograde Tract Tracing Studies," *J. Comp. Neurol.*, vol. 330, no. 2, pp. 195–220, 1993.

[11] N. Sun, M. D. Cassell, and S. Perlman, "Anterograde, transneuronal transport of herpes simplex virus type 1 strain H129 in the murine visual system.," *J. Virol.*, vol. 70, no. 8, pp. 5405–5413, 1996.

[12] P. Mombaerts *et al.*, "Visualizing an olfactory sensory map," *Cell*, vol. 87, no. 4, pp. 675–686, 1996.

[13] E. Gaggelli, E. Gaggelli, and P. C. Lauterbur, “Paramagnetic contrast agents in nuclear magnetic resonance medical imaging,” *Semin. Nucl. Med.*, vol. 13, no. 4, pp. 364–376, 1983.

[14] D. A. Cory, D. J. Schwartzentruber, and B. H. Mock, “Ingested manganese chloride as a contrast agent for magnetic resonance imaging,” *Magn. Reson. Imaging*, vol. 5, no. 1, pp. 65–70, 1987.

[15] R. G. Pautler, “In vivo, trans-synaptic tract-tracing utilizing manganese-enhanced magnetic resonance imaging (MEMRI),” *NMR Biomed.*, vol. 17, no. 8, pp. 595–601, 2004.

[16] K. Narita, F. Kawasaki, and H. Kita, “Mn and Mg influxes through Ca channels of motor nerve terminals are prevented by verapamil in frogs,” *Brain Res.*, vol. 510, no. 2, pp. 289–295, 1990.

[17] H. Tjälve, C. Mejàre, and K. Borg-Neczak, “Uptake and Transport of Manganese in Primary and Secondary Olfactory Neurones in Pike,” *Pharmacol. Toxicol.*, vol. 77, no. 1, pp. 23–31, 1995.

[18] H. Tjälve, J. Henriksson, J. Tallkvist, B. S. Larsson, and N. G. Lindquist, “Uptake of manganese and cadmium from the nasal mucosa into the central nervous system via olfactory pathways in rats,” *Pharmacol. Toxicol.*, vol. 79, no. 6, pp. 347–356, 1996.

[19] A. Takeda, Y. Kodama, S. Ishiwatari, and S. Okada, “Manganese transport in the neural circuit of rat CNS,” *Brain Res. Bull.*, vol. 45, no. 2, pp. 149–152, 1998.

[20] W. N. Sloot and J. B. P. Gramsbergen, “Axonal transport of manganese and its relevance to selective neurotoxicity in the rat basal ganglia,” *Brain Res.*, vol. 657, no. 1–2, pp. 124–132, 1994.

[21] Y. Y. Leung, L. Li, Y. Hui, and V. B. Kraus, “Colchicine --- update on mechanisms of action and therapeutic uses,” *Semin Arthritis Rheum*, vol. 45, no. 3, pp. 341–350, 2015.

[22] Y. J. Lin and A. P. Koretsky, “Manganese ion enhances T1-weighted MRI during brain activation: An approach to direct imaging of brain function,” *Magn. Reson. Med.*, vol. 38, no. 3, pp. 378–388, 1997.

[23] A. Takeda, S. Ishiwatari, and S. Okada, “In vivo stimulation-induced release of manganese in rat amygdala,” *Brain Res.*, vol. 811, no. 1–2, pp. 147–151, 1998.

[24] R. G. Pautler and A. P. Koretsky, “Tracing Odor-Induced Activation in the Olfactory Bulbs of Mice Using Manganese-Enhanced Magnetic Resonance Imaging,” *Neuroimage*, vol. 16, no. 2, pp. 441–448, 2002.

[25] A. Van Der Linden *et al.*, “In Vivo Manganese-Enhance Magnetic Resonance Imaging Reveals Connections and Functional Properties of the Songbird Vocal Control System,” *Neuroscience*, vol. 112, no. 2, pp. 467–474, 2002.

[26] K. S. Saleem *et al.*, “Magnetic resonance imaging of neuronal connections in the Macaque Monkey,” *Neuron*, vol. 34, no. 5, pp. 685–700, 2002.

[27] P. R. Allegrini and C. Wiessner, “Three-dimensional MRI of cerebral projections in rat brain in vivo after intracortical injection of MnCl2,” *NMR Biomed.*, vol. 16, no. 5, pp. 252–256, 2003.

[28] A. C. Silva, J. H. Lee, I. Aoki, and A. P. Koretsky, “Manganese-enhanced magnetic resonance imaging (MEMRI): Methodological and practical considerations,” *NMR Biomed.*, vol. 17, no. 8, pp. 532–543, 2004.

[29] C. W. Olanow, “Manganese-induced parkinsonism and parkinson’s disease,” *Ann. N. Y. Acad. Sci.*, vol. 1012, pp. 209–223, 2004.

[30] S. V. Chandra and G. S. Shukla, “Role of iron deficiency in inducing susceptibility to manganese toxicity,” *Arch. Toxicol.*, vol. 35, no. 4, pp. 319–323, 1976.

[31] G. L. Wolf and L. Baum, “Cardiovascular toxicity and tissue proton T1response to manganese injection in the dog and rabbit,” *Am. J. Roentgenol.*, vol. 141, no. 1, pp. 193–197, 1983.

[32] I. Aoki *et al.*, “Cell labeling for magnetic resonance imaging with the T1agent manganese chloride,” *NMR Biomed.*, vol. 19, no. 1, pp. 50–59, 2006.

[33] I. Tindemans, M. Verhoye, J. Balthazart, and A. Van Der Linden, “In vivo dynamic ME-MRI reveals differential functional responses of RA- and area X-projecting neurons in the HVC of canaries exposed to conspecific song,” *Eur. J. Neurosci.*, vol. 18, no. 12, pp. 3352–3360, 2003.

[34] V. Van Meir, M. Verhoye, P. Absil, M. Eens, J. Balthazart, and A. Van Der Linden, "Differential effects of testosterone on neuronal populations and their connections in a sensorimotor brain nucleus controlling song production in songbirds: A manganese enhanced-magnetic resonance imaging study," *Neuroimage*, vol. 21, no. 3, pp. 914–923, 2004.

[35] P. L. De Sousa, S. L. De Souza, A. C. Silva, R. E. De Souza, and R. M. De Castro, "Manganese-enhanced magnetic resonance imaging (MEMRI) of rat brain after systemic administration of MnCl2: Changes in T1 relaxation times during postnatal development," *J. Magn. Reson. Imaging*, vol. 25, no. 1, pp. 32–38, 2007.

[36] J. M. Simmons, Z. S. Saad, M. J. Lizak, M. Ortiz, A. P. Koretsky, and B. J. Richmond, "Mapping Prefrontal Circuits In Vivo with Manganese-Enhanced Magnetic Resonance Imaging in Monkeys," *J. Neurosci.*, vol. 28, no. 30, pp. 7637–7647, 2008.

[37] X. Yu, Y. Z. Wadhgiri, D. H. Sanes, and D. H. Turnbull, "In vivo auditory brain mapping in mice with Mn-enhanced MRI Xin," *Nat. Neurosci.*, pp. 961–968, 2005.

[38] Y.-T. Kuo, A. H. Herlihy, P.-W. So, and J. D. Bell, "Manganese-enhanced magnetic resonance imaging (MEMRI) without compromise of the blood–brain barrier detects hypothalamic neuronal activity in vivo," *NMR Biomed.*, vol. 19, pp. 1028–1034, 2006.

[39] K. D. B. Smith, V. Kallhoff, H. Zheng, and R. G. Pautler, "In vivo axonal transport rates decrease in a mouse model of Alzheimer's disease," *Neuroimage*, vol. 35, no. 4, pp. 1401–1408, 2007.

[40] J. P. van der Zijden, O. Wu, A. van der Toorn, T. P. Roeling, R. L. A. W. Bleys, and R. M. Dijkhuizen, "Changes in neuronal connectivity after stroke in rats as studied by serial manganese-enhanced MRI," *Neuroimage*, vol. 34, no. 4, pp. 1650–1657, 2007.

[41] M. Bilgen, N. Dancause, B. Al-Hafez, Y. Y. He, and T. M. Malone, "Manganese-enhanced MRI of rat spinal cord injury," *Magn. Reson. Imaging*, vol. 23, no. 7, pp. 829–832, 2005.

[42] K. Chuang, J. H. Lee, A. C. Silva, L. Belluscio, and A. P, "Manganese Enhanced MRI Reveals Functional Circuitry in Response to Odorant Stimuli," *Neuroimage*, vol. 44, pp. 363–372, 2009.

[43] J. Tucciarone, K. H. Chuang, S. J. Dodd, A. Silva, G. Pelled, and A. P. Koretsky, “Layer specific tracing of corticocortical and thalamocortical connectivity in the rodent using manganese enhanced MRI,” *Neuroimage*, vol. 44, no. 3, pp. 923–931, 2009.

[44] C. A. Massaad and R. G. Pautler, *Magnetic Resonance Neuroimaging Methods and Protocols - Manganese-Enhanced Magnetic Resonance Imaging (MEMRI)*, vol. 711. 2010.

[45] T. Inoue, T. Majid, and R. G. Pautler, “Manganese enhanced MRI (MEMRI): Neurophysiological applications,” *Rev. Neurosci.*, vol. 22, no. 6, pp. 675–694, 2011.

[46] A. C. Silva, “Using manganese-enhanced MRI to understand BOLD,” *Neuroimage*, vol. 62, no. 2, pp. 1009–1013, 2012.

[47] K. H. Chuang and A. P. Koretsky, “Accounting for nonspecific enhancement in neuronal tract tracing using manganese enhanced magnetic resonance imaging,” *Magn. Reson. Imaging*, vol. 27, no. 5, pp. 594–600, 2009.

[48] P. Svehla, A. Bédécarrats, C. Jahn, R. Nargeot, and L. Ciobanu, “Intracellular manganese enhanced MRI signals reflect the frequency of action potentials in Aplysia neurons,” *J. Neurosci. Methods*, vol. 295, pp. 121–128, 2018.

[49] B. T. Bedenk *et al.*, “Mn2+dynamics in manganese-enhanced MRI (MEMRI): Cav1.2 channel-mediated uptake and preferential accumulation in projection terminals,” *Neuroimage*, vol. 169, no. August 2017, pp. 374–382, 2018.

[50] J. H. Lee, A. C. Silva, H. Merkle, and A. P. Koretsky, “Manganese-enhanced magnetic resonance imaging of mouse brain after systemic administration of MnCl2: Dose-dependent and temporal evolution of T1contrast,” *Magn. Reson. Med.*, vol. 53, no. 3, pp. 640–648, 2005.

[51] T. L. Roth, D. Nayak, T. Atanasijevic, A. P. Koretsky, L. L. Latour, and D. B. McGavern, “Transcranial amelioration of inflammation and cell death after brain injury,” *Nature*, vol. 505, no. 7482, pp. 223–228, 2014.

[52] T. Atanasijevic, N. Bouraoud, D. B. Mcgavern, and A. P. Koretsky, “NeuroImage Transcranial manganese delivery for neuronal tract tracing using MEMRI,” *Neuroimage*, vol. 156, no. May, pp. 146–154, 2017.

[53] S. I. Mok, J. P. Munasinghe, and W. S. Young, “Infusion-based manganese-enhanced MRI: A new imaging technique to visualize the mouse brain,” *Brain Struct. Funct.*, vol. 217, no. 1, pp. 107–114, 2012.

[54] M. R. Sepúlveda *et al.*, “Evaluation of manganese uptake and toxicity in mouse brain during continuous MnCl2 administration using osmotic pumps,” *Contrast Media Mol. Imaging*, vol. 7, no. 4, pp. 426–434, 2012.

[55] O. Eschenko, S. Canals, I. Simanova, M. Beyerlein, Y. Murayama, and N. K. Logothetis, “Mapping of functional brain activity in freely behaving rats during voluntary running using manganese-enhanced MRI: Implication for longitudinal studies,” *Neuroimage*, vol. 49, no. 3, pp. 2544–2555, 2010.

[56] D. S. Poole, N. Doorenweerd, J. J. Plomp, A. Mahfouz, M. J. T. Reinders, and L. van der Weerd, “Continuous infusion of manganese improves contrast and reduces side effects in manganese-enhanced magnetic resonance imaging studies,” *Neuroimage*, vol. 147, no. October 2016, pp. 1–9, 2017.

[57] D. A. Vousden *et al.*, “Continuous manganese delivery via osmotic pumps for manganese-enhanced mouse MRI does not impair spatial learning but leads to skin ulceration,” *Neuroimage*, vol. 173, no. March, pp. 411–420, 2018.

[58] E. L. Bearer, B. C. Manifold-Wheeler, C. S. Medina, A. G. Gonzales, F. L. Chaves, and R. E. Jacobs, “Alterations of functional circuitry in aging brain and the impact of mutated APP expression,” *Neurobiol. Aging*, vol. 70, pp. 276–290, 2018.

[59] P. Baumgartner, M. El Amki, O. Bracko, A. R. Luft, and S. Wegener, “Sensorimotor stroke alters hippocampo-thalamic network activity,” *Sci. Rep.*, vol. 8, no. 1, p. 15770, 2018.

[60] L. R. Qiu *et al.*, “Mouse MRI shows brain areas relatively larger in males emerge before those larger in females,” *Nat. Commun.*, vol. 9, no. 1, 2018.

[61] G. Paxinos and C. Watson, *The Rat Brain In Stereotaxic Coordinates Seventh Edition*, 7th ed. 2014.

[62] S. M. Smith *et al.*, “Advances in functional and structural MR image analysis and implementation as FSL,” *Neuroimage*, vol. 23, no. SUPPL. 1, pp. 208–219, 2004.

[63] R. W. Cox, “AFNI: Software for analysis and visualization of functional magnetic resonance neuroimages,” *Comput. Biomed. Res.*, vol. 29, no. 3, pp. 162–173, 1996.

[64] “10 Signs Of Illness In Rats You Should Know - RatCentral.” [Online]. Available: https://www.ratcentral.com/signs-illness-rats/. [Accessed: 14-Nov-2018].